Department of Precision and Microsystems Engineering

The transmission of pump induced pressure disturbances to nano-precision instrumentation

Dennis Koens

Report no	: 2023.081
Coach	: Dick Laro
Professor	: Ron van Ostayen
Specialisation	: Mechatronic System Design
Type of report	: Master Thesis
Date	: 4 September 2023

TU Delft Delft University of Technology

The transmission of pump induced pressure disturbances to nano-precision instrumentation

by

Dennis Koens

to obtain the degree of Master of Science
at the Delft University of Technology,
to be defended publicly on
Monday 18 September, 2023 at 10:00 AM.

TU Delft

Abstract

High-tech systems are subjected to strict temperature requirements. Therefore temperature control using cooling water is vital for thermal stability. Unfortunately, components like pumps and fluid couplings generate flow disturbances, resulting in mechanical vibrations that influence the performance of the system. This research focusses on the propagation of pump induced pressure oscillations to nano-precision instrumentation. A generic vibration isolated precision system has been considered. The system contains a cooling conduit, which is connected to a mechanically isolated pump by viscoelastic tubing. Pressure disturbances are transmitted to the system due to fluid-structure interaction at curved tubes in the cooling conduit. Luckily, viscoelastic tubes are proven to attenuate pressure oscillations. A model has been presented to predict the system disturbance due to pressure oscillations produced by a pump. An experimental setup has been considered to validate the model. The setup represents a simple mechatronic system. Results show that the model provides a decent qualitative description of the spectral disturbance behaviour, however it is only capable of giving an order of magnitude estimation of the overall disturbance. Based on the knowledge gained in this research, possible design improvements can be proposed. These include changing the dimensions of the viscoelastic tubes and altering the mechanical eigenfrequencies of the cooling conduit.

Contents

1 Introduction

High-precision systems are a class of mechatronic systems that are subjected to very strict positioning requirements, sometimes in the order of nanometers. These systems are, for instance, developed for the semiconductor industry or the biomedical industry. The waver stepper machines developed by ASML are a good example of a high precision proses in which ever increasing performance is desired. However, increasing the performance of precision systems comes with a lot of challenges. Every precision system experiences disturbances that have a negative effect on the system's performance. These include floor vibrations, acoustic noise, electrical noise and dynamic noise.

Error budgeting is often used to evaluate how much a disturbance is allowed to contribute to the total error. Most disturbances are stochastic of nature. Therefore, they are often modelled using their Power Spectral Density (PSD). The PSD is a measure for the spectral energy distribution of a signal. The PSD of the total disturbance is the sum of the PSD's of the individual disturbance sources. This approach allows for frequency dependent error budgeting, which is also referred to as dynamic error budgeting (DEB) [10, 22]. DEB enables the designer to identify components in the machine that limit its performance.

A generic representation of a precision system is shown in figure 1.1. The system consists of a base that is mechanically isolated from the floor by using vibration isolation. The system contains a positioning stage which is used to measure or manipulate a sample. By doing this, a certain amount of heat will be generated and dissipated into the system, resulting in thermal deformations that will hurt the system's performance. Deformations caused by heating can partly be avoided by careful design, but ultimately some thermal effects will remain. Therefore, strict temperature requirements are imposed on most systems. The use of cooling water is vital to meet these requirements. The cooling pump may be placed meters away from the precision system, so viscoelastic tubes are commonly used to transport the fluid from the pump to the system. These tubes are often referred to as dynamic links.

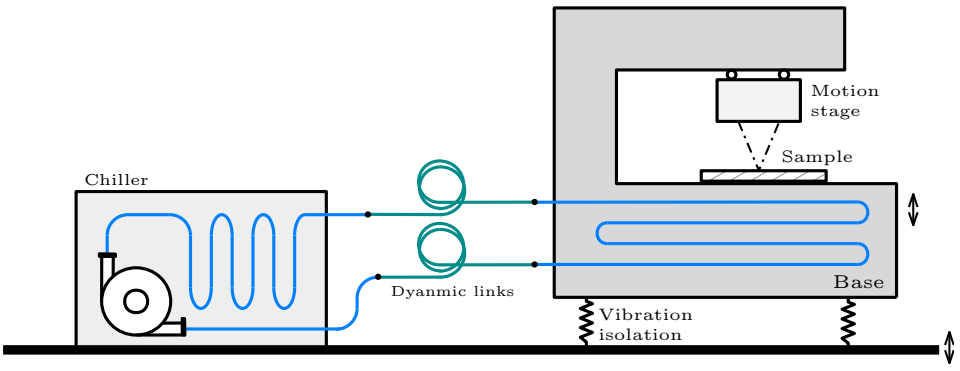

Figure 1.1: Generic representation of a precision system with liquid cooling. The chiller consists of a pump and a heat exchanger

Unfortunately, flowing water creates disturbances, referred to as flow induced vibrations (FIV). These vibrations can generate dominant disturbances on precision instrumentation. FIV is generally caused by unsteady flow originating from sharp corners, protruding parts, tube branches or diameter changes. For ex-

ample, most fluid couplings do not have a smooth inner surface. The unsteady flow creates acoustic pressure pulsations that will propagate through the fluid in the tube. The pressure pulsations are generated by an acoustic feedback loop in which flow separation at the sharp edges couples with the acoustic flow field, resulting in an unsteady vorticity field [16, 27]. The vorticity field will decay rapidly as it moves downstream with the velocity of the fluid, however, the internal pressure acoustic field decays rather slowly and will propagate down the pipe at the speed of sound, where the fluid in the tube will act as an acoustic waveguide [5].

For designers it is important to be able to predict the magnitude of disturbances generated by FIV. Therefore it is vital to understand the mechanisms that are responsible for the generation and propagation of fluid pressure pulsations and mechanical vibrations in piping systems. The focus of this research will be on the propagation of pump induced vibrations to nano-precision instrumentation by using dynamic error budgeting. Hereby the pump will act as an acoustic pressure disturbance source. FIV produced by other components in the circuit will not be considered. The research objective is formulated as follows:

Predicting the transmission of pump induced vibrations to nano-precision instrumentation by using dynamic error budgeting

DEB offers a convenient method to gain insight into the spectral error contribution of a disturbance. A model will be developed to compute the disturbance magnitude induced by a known pressure disturbance at the pump outlet. An experimental setup will be considered to verify the model. A schematic overview of the experimental setup is shown in figure 1.2. This setup is a representation of the simplified precision system as shown in figure 1.1 but without a motion stage. The setup has been designed such that pressure pulsations generated by the pump are the predominant disturbance source. This means that errors induced by floor vibrations or acoustic noise though the air will be limited.

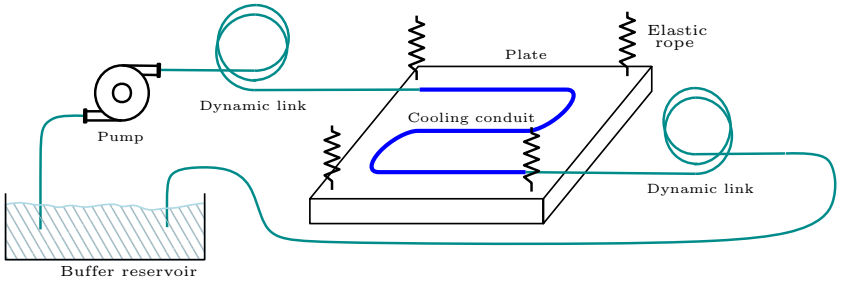

Figure 1.2: Schematic overview of the experimental setup. The elastic ropes are depicted by the 4 springs and the dynamic links are shown in a different colour compared to the steel conduit on the plate.

The setup consists of a plate with a cooling conduit that is suspended to the ceiling by four elastic ropes. These ropes provide the vibration isolation to the system. The in- and outlet of the conduit will be connected to a pump by dynamic links. Vibrations of the plate will be measured by an accelerometer. The plate acceleration will be used as a measure for the disturbance magnitude on the system. For a precision machine, the acceleration magnitude stays typically well below $1\,\mathrm{mm/s^2}$. At 100Hz, this results into a displacement, x, in the order of nanometres, as shown in the calculation below.

$$x = \frac{\ddot{x}}{\omega^2} = \frac{1\times10^{-3}\,\mathrm{m/s^2}}{(2\pi\cdot100\,\mathrm{Hz})^2} = 2.53\times10^{-9}\,\mathrm{m}$$

The main matter of this report is structured in three chapters. Chapter 2 covers the fluid dynamics in a liquid-filled cooling tube. An analytical model is devised to model the pressure wave propagation in elastic or viscoelastic tubes. This model will be used to compute the fluid behaviour in the dynamic links. Chapter 3 discusses the interaction between the pressure acoustics in the fluid and the mechanics of the tube. A finite element model has been developed to predict the reaction force as a result of an excitation pressure. Both chapter 2 and 3 are concluded with an experiment to validate the theory. Chapter 4 covers the transmission of pump induced vibrations in a mechatronic application by using the setup shown in figure 1.2. Here, the measurement results will be compared to the model. Based on the knowledge gained in the research some basic design guideline can be drafted. These are covered in the discussion in chapter 5. Lastly, the report is finished with a conclusion and recommendations in chapter 6.

2

Fluid transients in liquid filled tubes

Pressure pulsations generated by a pump will propagate through the liquid-filled tubes of a cooling circuit. The dynamics of a fluid conveyed through a circular tube will be covered in this chapter. The theory discussed is especially useful for modelling the fluid behaviour in the dynamic links. The presence of these links has a big impact on a system. It is shown that the viscoelastic tube material of the links imposes damping on the fluid pressure. The one-dimensional pressure propagation through a tube is governed by the same physics used to model water hammer. Water hammer is a pressure surge which occurs when a fluid in motion is forced to stop or change direction. This commonly happens due to a rapid closure of a valve. The tube material and thickness have an influence on the fluid dynamics.

The chapter is structured as follows. Water hammer theory is introduced in section 2.1. Section 2.2 discusses transmission line modelling. This a solution method that can be used to solve the water hammer equations by using an electrical analogy. The fluid behaviour for a tube consisting of one or multiple sections are discussed in section 2.3 and 2.4. Furthermore, methods for modelling viscoelastic tubes are covered in section 2.5 and the chapter is concluded with an experimental validation.

2.1. Water hammer

2.1.1. Joukowsky equation

The present water hammer theory is based on the work of Joukowsky and Allevi. Joukowsky derived a formula that relates a change in velocity ΔV to a change in pressure ΔP [15, 7, 4]

$$\Delta P = \rho a \Delta V \tag{2.1}$$

where ρ = fluid density and a = acoustic wave speed. This formula is commonly called the Joukowsky equation or the "fundamental equation of water hammer". The calculation of the acoustic wave speed will be discussed in chapter 2.1.3.

The formula is useful for calculating the magnitude of a pressure surge created by a sudden closure of a valve in a pipe with fluid flow. When the valve is closed a pressure front with magnitude ΔP will travel upstream and a pressure front with magnitude $-\Delta P$ will move downstream. The Joukowsky equation is very useful as a first approximation. However, one should be aware of its limitations. The equation does not take the effect of friction into account, the height of the pressure surge will decrease when travelling over a large distance and lastly, the result will be less accurate when the velocity change ΔV is close to the acoustic wave speed c due to non-linear effects. [9]

2.1.2. Fundamental equations of 1D water hammer

The one dimensional nature of pipe networks allows for an one-dimensional description of the transient fluid flow. This assumption can be made because the axial fluxes of mass, momentum and energy are far greater than their radial counterparts. The transient behaviour is governed by a continuity and momentum equation [7, 4, 1]

$$\frac{\partial V}{\partial x} + \frac{1}{\rho a^2}\frac{\partial P}{\partial t} = 0 \tag{2.2}$$

$$\frac{\partial V}{\partial t} + \frac{1}{\rho}\frac{\partial P}{\partial x} = 0 \tag{2.3}$$

in which x = the spatial coordinate along the pipeline, t = time. Throughout this report, zero-mean flow will be assumed. This means that only the harmonic fluctuations on top of the mean flow and mean pressure will be considered. The variables P and V therefore represent the dynamic pressure and dynamic flow velocity.

Equations 2.2 and 2.3 are often referred to as the fundamental equations for 1D water hammer. Viscous friction in the fluid and gravity have been neglected in these equations. The fundamental equations of 1D-water hammer contain all the physics necessary to model wave propagation in complex pipe systems. The equations have been derived by applying the principles of mass and momentum to a control volume. An alternative derivation could be performed by applying the unidirectional and axisymmetric assumptions to the compressible Navier-Stokes equations. The equations have been simplified by assuming that the Mach number, $M = V/c$ is a lot smaller than 1. A detailed derivation can be found in [7].

2.1.3. Pressure wave speed

The pressure wave speed can be expressed as [7]

$$\frac{1}{a^2} = \frac{d\rho}{dP} + \frac{\rho}{A}\frac{dA}{dP} \tag{2.4}$$

The first term on the right hand side represents the effect of fluid comprehensibility and the second term represents the pipe elasticity. The formula can be reduced to $\frac{1}{a^2} = \frac{d\rho}{dP}$ when assuming that the pipe is rigid. Likewise, it can be reduced to $\frac{1}{a^2} = \frac{\rho}{A}\frac{dA}{dP}$ when the effect of fluid compressibility is small compared to the elasticity of the pipe.

Korteweg [3] rewrote the first term using the state equation and rewrote the second term using the mechanics of the tube. By doing this he derived to the following relation, which is usually referred to as the Korteweg equation [15, 7]

$$a = \sqrt{\frac{K}{\rho}\left(1 + \frac{DK}{eE}\right)^{-1}} \tag{2.5}$$

In his derivation Korteweg ignored the axial stresses in the pipeline and the inertia of the pipe. These assumption mean that Korteweg effectively modelled the pipe as a series of massless rings expanding and contracting due to the fluid pressure inside. This assumption is valid when the pipe is supported with expansion joints throughout its length.

The bulk modulus of elasticity is a measure of how resistant a substance is to compression. It is defined as

$$K = \rho\frac{dP}{d\rho} \tag{2.6}$$

Meaning that the first term can be rewritten as $\frac{d\rho}{dP} = \frac{\rho}{K}$. The inverse of this relation is called the state equation

An increase in pressure causes an increase in the hoop stress of the massless ring according to

$$DdP = 2ed\sigma \tag{2.7}$$

The change in area as the result of a circumferential strain can be written as

$$dA = \frac{1}{2}\pi D^2 d\xi \tag{2.8}$$

This is equivalent to

$$dA = 2Ad\xi \tag{2.9}$$

Using the elastic stress-strain relation $d\xi = d\sigma/E$ and equations 2.7 and 2.9 one can write

$$\frac{\rho}{A}\frac{dA}{dP} = \frac{D\rho}{eE} \tag{2.10}$$

where D = the tube's inner diameter, K = the bulk modulus of elasticity, e = the tube thickness and E = the Young's modulus of the tube. Substituting equation 2.10 and the state equation into equation 2.4 gives Korteweg's relation. Korteweg's relation can be extended to problems where the axial stress cannot be neglected. This can be done by including the Poisson effect into the stress-strain relationship, resulting into the following wave speed formula

$$a = \sqrt{\frac{K}{\rho}\left(1 + \Psi\frac{DK}{eE}\right)^{-1}} \tag{2.11}$$

The correction factor Ψ accounts for the different support conditions. Three standard support conditions are considered (1) the pipe is anchored with expansion joints throughout its length, (2) the pipe is anchored throughout against axial motion and (3) the pipe is anchored at the upstream end. Support condition (1) corresponds to the case derived by Korteweg ($\Psi = 1$), with the axial stress being neglected. For case (2) it holds that $\Psi = 1 - \nu^2$ and for case (3) it holds that $\Psi = 1 - \frac{1}{2}\nu$. A derivation for these support cases can be found in [4].

2.2. Transmission line modelling

The water hammer equations are usually solved with numerical methods of which the method of characteristic (MOC) is the most popular. This technique solves the water hammer equations in the time domain for certain initial conditions. However, for this research we are rather interested in the frequency domain response. For this, transmission line modelling offers an analytical way to solve the water hammer 2-equation model in the frequency domain. This method has originally been developed to model long electrical lines, but it can also be used to model fluid transmission lines [8, 23].

2.2.1. Electrical analogy

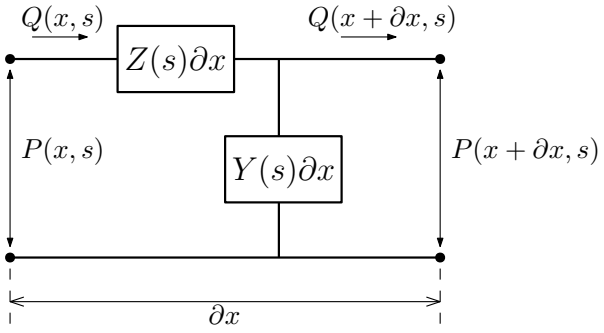

Figure 2.1: Transmission line element of infinitesimal length ∂x. The analogy with a fluid transmission line has be made by replacing voltage with pressure P and electrical current with fluid flow Q.

The circuit in figure 2.1 represents a transmission line element of infinitesimal length. A transmission line consists of an infinite number of these elements connected after one another. A transmission line can be fully described by two complex functions of frequency: the series impedance, $Z(s)$, and the shunt admittance, $Y(s)$. The analogy with a fluid transmission line can be made by replacing voltage with pressure P and electrical current with fluid flow Q [25, 14]. From applying Kirchoffs node and loop laws it follows that

$$\frac{\partial P(s)}{\partial x} = -Z(s)Q(s) \qquad \frac{\partial Q(s)}{\partial x} = -Y(s)P(s) \tag{2.12}$$

This system of equations can be solved and the solution can be written in a convenient matrix form

$$\begin{bmatrix} P(x,s) \\ Q(x,s) \end{bmatrix} = \begin{bmatrix} \cosh\Gamma(s)x & -Z_c(s)\sinh\Gamma(s)x \\ -Z_c(s)^{-1}\sinh\Gamma(s)x & \cosh\Gamma(s)x \end{bmatrix} \begin{bmatrix} P_i(s) \\ Q_i(s) \end{bmatrix} \tag{2.13}$$

where

$$\Gamma(s) = \sqrt{Z(s)Y(s)} \tag{2.14}$$

$$Z_c(s) = \sqrt{Z(s)/Y(s)} \tag{2.15}$$

Γ and Z_c are respectively called the propagation constant and the characteristic impedance. Equation 2.13 describes the relation of pressure and flow between the input and a cross-section at coordinate x, see appendix A for a detailed derivation.

2.2.2. Model impedances

The propagation constant (Γ) and the characteristic impedance (Z_c) need to be calculated in order to determine the frequency response of a fluid line. The water hammer equations can be written into the same form as equations 2.12 in order to determine the model impedances $Y(s)$ and $Z(s)$. Using the relation for velocity and flow ($q = VA$) and taking the Laplace transform gives

$$\frac{\partial P(s)}{\partial x} = -\frac{\rho s}{A} Q(s) \qquad \frac{\partial Q(s)}{\partial x} = -\frac{As}{a^2\rho} P(s) \tag{2.16}$$

So, the parameters $Y(s)$ and $Z(s)$ are

$$Z(s) = \frac{\rho s}{A} \qquad Y(s) = \frac{As}{a^2\rho} \tag{2.17}$$

The propagation factor Γ and characteristic impedance Z_c become

$$\Gamma(s) = \sqrt{\frac{\rho s}{A}\frac{As}{a^2\rho_0}} = \sqrt{\frac{s^2}{a^2}} = \frac{s}{a} \tag{2.18}$$

$$Z_c(-) = \sqrt{\frac{\frac{\rho s}{A}}{\frac{As}{a^2\rho}}} = \sqrt{\frac{\rho^2 a^2}{A^2}} = \frac{\rho a}{A} \tag{2.19}$$

The model impedances above assume the the fluid line to be lossless, meaning that the fluid is inviscid and that there is no heat transfer between the fluid and the tube walls. The propagation factor and characteristic impedance for a fluid line with viscous friction and heat transfer is derived in [25, 14].

2.3. Single section fluid column

The pressure transfer function for a fluid column with the same material and a uniform tube diameter and thickness will be considered in this section. A schematic of a transmission line is depicted in figure 2.2. The line is terminated with a load impedance. This impedance is needed to impose a boundary condition at the end of the line. The flow at the output is zero when the line is blocked. This means that the load impedance should be infinite. Contrary, when the line is open at the output the pressure should be zero and the load impedance also equals zero.

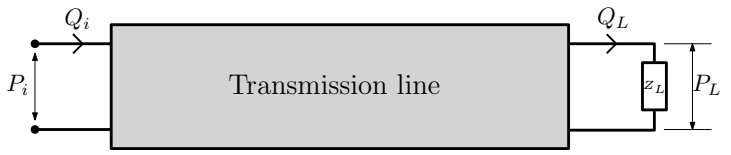

Figure 2.2: Schematic representation of a transmission line with load impedance Z_L. The block represents an infinite number of line elements as shown in figure 2.1.

The transfer function between the pressure at a certain point x (P_x) and the input potential (P_i) can be calculated using the following relation $P_x/P_i = (P_x/P_L)(P_L/P_i)$. The fraction P_x/P_i cannot be calculated directly since the load impedance should be involved in the calculation in order to relate flow to pressure at the

end of the tube. Otherwise one would end up with an expression in terms of both the pressure and current. Writing out P_x/P_i gives

$$\frac{P_x(s)}{P_i(s)} = \frac{\sinh\big(\Gamma(s)(l-x)\big)+\frac{Z_L}{Z_c}\cosh\big(\Gamma(s)(l-x)\big)}{\sinh\big(\Gamma(s)l\big)+\frac{Z_L}{Z_c}\cosh\big(\Gamma(s)l\big)} \tag{2.20}$$

A detailed derivation can be found in appendix B. The transfer functions for a closed and open fluid line are respectively

$$\text{closed tube}: \quad Z_L = \infty \quad \rightarrow \quad \frac{P_x(s)}{P_i(s)} = \frac{\cosh\big(\Gamma(s)(l-x)\big)}{\cosh\big(\Gamma(s)l\big)} \tag{2.21}$$

$$\text{open tube}: \quad Z_L = 0 \quad \rightarrow \quad \frac{P_x(s)}{P_i(s)} = \frac{\sinh\big(\Gamma(s)(l-x)\big)}{\sinh\big(\Gamma(s)l\big)} \tag{2.22}$$

Closed fluid transmission lines are not relevant for this research, because a flow is required to cool the system. Therefore, only open fluid lines will be considered. Expression 2.22 can be written in terms of two sin-functions when plugging the propagation factor Γ into the equation and by using that $\sinh(ix) = i\sin(x)$.

$$\frac{P_x(s)}{P_i(s)} = \frac{\sin\big(\frac{\omega}{a}(l-x)\big)}{\sin\big(\frac{\omega}{a}l\big)} \tag{2.23}$$

A single section open tube with the properties listed table 2.1 is now considered as an example. The frequency response between $x = 0$ and $x = 0.6L$ is shown in figure 2.3.

Parameter	**Quantity**	**Value**
Fluid properties		
K	Bulk modulus of elasticity	2.2 GPa
ρ	Density	997 kg/m^3
Tube properties		
l	length	3 m
D	inner diameter	6 mm
e	wall thickness	1 mm
E	Young's modulus	205 GPa
Ψ	Support correction factor	1

Table 2.1: Properties of a fluid-filled, single-section tube.

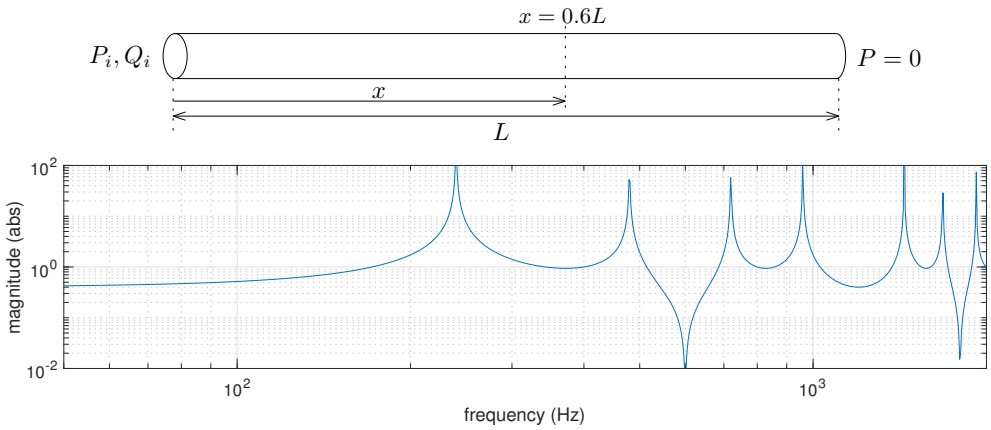

Figure 2.3: Frequency response function between $x = 0$ and $x = 0.6L$ for a closed and open tube

The magnitude shows both resonances and anti-resonances. It can be seen that the first resonance only occurs at 240Hz. The resonance and anti-resonance frequencies can be found by equating the nominator and denominator to zero, resulting in the following expressions

$$\text{poles:} \quad f_0 = n\frac{a}{2l} \qquad \text{with} \quad n = 1,2,3,... \tag{2.24}$$

$$\text{zeros:} \quad f_0 = n\frac{a}{2(l-x)} \qquad \text{with} \quad n = 1,2,3,... \tag{2.25}$$

Note that the poles and zeros may cancel each other for certain values of x. The frequency peaks turn out to be independent of the position at which the transfer function is probed. Furthermore, the formulas show that an increase in length results in shift of the poles and zeros to the left. The same holds for a decrease in Young's modulus, because a lower Young's modulus results in a higher wavespeed according to formula 2.11.

The frequency response over every position on the tube x from the previous example is plotted in figure 2.4. The figure shows how the poles and zeros move over the position x. The poles and zeros will cancel each other for certain frequencies. The pressure distribution at different frequencies is depicted in figure 2.5. At low frequencies below the first resonance, the pressure amplitude will drop linearly from the input pressure to zero. The differential pressure drop over the length of the fluid line is used to accelerate the fluid. The first four mode shapes are also shown in the figure.

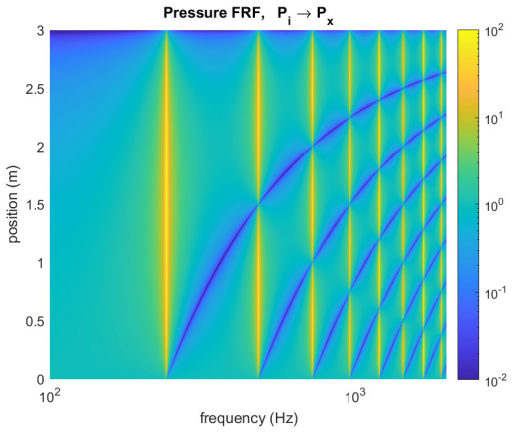

Figure 2.4: Frequency response function between p_i and p_x for different positions of x. The shift of the resonance and anti-resonance frequencies can clearly be seen.

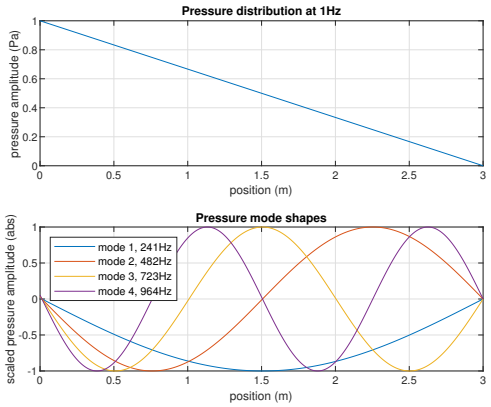

Figure 2.5: Pressure distribution along the length of the tube. The top plot shows the pressure distribution at 1Hz and the bottom plot shows the mode shapes of the first 4 modes.

The formulas above show that the tube length after probing point x is relevant for the dynamic behaviour. However, any additional tubing placed before the input (at the probing point of P_i and Q_i) is irrelevant for the fluid behaviour.

2.4. Multi-section fluid column

A dynamic link often consists of multiple sections with different diameters or different materials. The transmission line method can also be used to model flow circuits containing multiple sections. This can be achieved by drafting a separate transfer matrix for every sections and by multiplying them with each other [12]

$$\begin{bmatrix} P(x,s) \\ Q(x,s) \end{bmatrix} = [T_n][T_{n-1}]\cdots[T_2][T_1]\begin{bmatrix} P_i(s) \\ Q_i(s) \end{bmatrix} \tag{2.26}$$

with

$$T_n = \begin{bmatrix} \cosh\Gamma_n(s)x & -Z_{cn}(s)\sinh\Gamma_n(s)x \\ -Z_{cn}(s)^{-1}\sinh\Gamma_n(s)x & \cosh\Gamma_n(s)x \end{bmatrix} \tag{2.27}$$

As an an example a two-section tube will be considered. Using the relation $P_x/P_i = (P_x/P_l)(P_L/P_i)$ the following transfer function can be derived.

$$\frac{P_x}{P_i} = \frac{\left(\cosh(\Gamma_1 l_{1x})\cosh(\Gamma_2 l_{2x}) + \frac{Z_{c1}}{Z_{c2}}\sinh(\Gamma_1 l_{1x})\sinh(\Gamma_2 l_{2x})\right) - \frac{1}{Z_L}\left(Z_{c1}\cosh(\Gamma_2 l_{2x})\sinh(\Gamma_1 l_{1x}) + Z_{c2}\cosh(\Gamma_1 l_{1x})\sinh(\Gamma_2 l_{2x})\right)}{\left(\cosh(\Gamma_1 l_1)\cosh(\Gamma_2 l_2) + \frac{Z_{c1}}{Z_{c2}}\sinh(\Gamma_1 l_1)\sinh(\Gamma_2 l_2)\right) - \frac{1}{Z_L}\left(Z_{c1}\cosh(\Gamma_2 l_2)\sinh(\Gamma_1 l_1) + Z_{c2}\cosh(\Gamma_1 l_1)\sinh(\Gamma_2 l_2)\right)} \tag{2.28}$$

with

$$l_{1x} = \begin{cases} l_1 - x, & \text{if } x \le l_1 \\ 0, & \text{if } x > l_1 \end{cases} \tag{2.29}$$

$$l_{2x} = \begin{cases} l_2, & \text{if } x \le l_1 \\ l1 + l2 - x, & \text{if } x > l_1 \end{cases} \tag{2.30}$$

The transfer functions for an open fluid line ($Z_L = 0$) is

$$\frac{P_x}{P_i} = \frac{Z_{c1}\cosh(\Gamma_2 l_{2x})\sinh(\Gamma_1 l_{1x}) + Z_{c2}\cosh(\Gamma_1 l_{1x})\sinh(\Gamma_2 l_{2x})}{Z_{c1}\cosh(\Gamma_2 l_2)\sinh(\Gamma_1 l_1) + Z_{c2}\cosh(\Gamma_1 l_1)\sinh(\Gamma_2 l_2)} \tag{2.31}$$

The same derivation can be made for a fluid column consisting of three sections. However, the derivation for a tube with more than two section will become very long and tedious. Alternatively, the one-dimensional water hammer equations can also be solved by using a finite element solver, see appendix G.1.

A two-section open tube with properties listed in the table below has been considered. The frequency response between $x = 0$ and $x = 0.6(l1 + l2)$ is shown in figure 2.6.

Parameter	**Quantity**	**Value**
Tube properties		
l_1	length, 1st section	1.5 m
l_2	length, 2nd section	1.5 m
D_1	diameter, 1st section	12 mm
D_2	diameter, 2nd section	6 mm

Table 2.2: Properties of a fluid-filled, two-section tube. The bulk modulus of elasticity K, density ρ, wall thickness e, Young's modulus E and support correction factor Ψ remain the same as in table 2.1 for both sections.

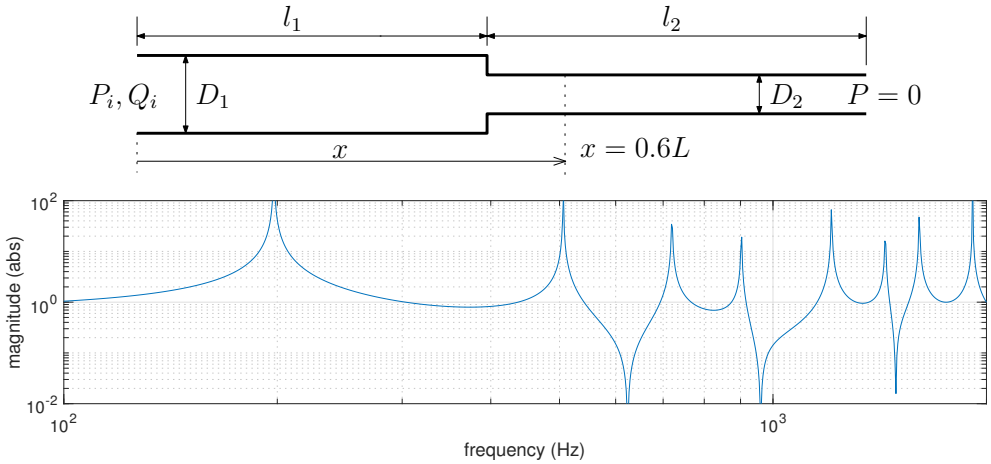

Figure 2.6: Frequency response function between $x = 0$ and $x = 0.6L$ for an open tube consisting of two sections

2.5. Tube viscoelasticity

The flexible links between the pump and the fluid conduit are usually made of a viscoelastic polymer, such as silicone rubber. The viscoelasticity of the tube has a significant influence on the pressure wave propagation in the fluid. Several authors [2] have stated that the damping due to fluid viscosity is negligible compared to damping induced by the viscoelasticity of the tube. This has also been proven in appendix C. It is common practise to make the flexible links longer than needed in order to dampen out pressure pulsations from the pump, but it is unknown how much additional length is needed to dampen out the pulsations to a certain level.

Viscoelastic materials exhibit both viscous and elastic behaviour under deformation. The behaviour of a viscoelastic material can be described by the dynamic Young's modulus, which is the ratio of stress to strain under vibratory conditions. This complex variable can be expressed as

$$E(i\omega) = E'(\omega) + iE"(\omega) \tag{2.32}$$

with E' being the storage modulus, representing the elastic part and $E"$ the loss modulus, representing the viscous part. Both parameters can be frequency dependent. The ratio between the storage modulus and loss tangent is defined as the loss tangent $\tan(\delta) = \frac{E"}{E'}$. Loss modulus data is usually reported in terms of $\tan(\delta)$. For this research, the tube material is assumed to be linear viscoelastic, meaning that the stress is linearly proportional to the strain rate. Assuming linear viscoelasticity is generally excepted when considering small deformations. [2, 11, 13]

Viscoelastic materials can be modelled by representing the material as a combination of springs and dampers. The stress strain behaviour of a spring element is described by Hooke's law according to

$$\sigma = E\epsilon \tag{2.33}$$

The linear viscous response of a damper is described by Newton's law

$$\sigma = \eta \partial\epsilon/\partial t \tag{2.34}$$

Two well-known representations are the Maxwell model and the Kelvin-Voigt model. The Maxwell model consists of a spring and dashpot in series and the Kelvin-Voigt model is build up with both elements in parallel. A schematic representation of both models with their respective Young's moduli is shown below. [19]

Maxwell

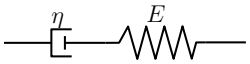

$E^*(j\omega) = \frac{j\omega E\eta}{E+j\omega\eta}$

Kelvin-Voigt

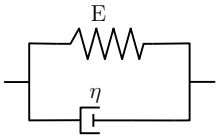

$E^*(j\omega) = E + j\omega\eta$

Often times more elaborate models such as the Maxwell-Weichert model or the generalized Kelvin-Voigt model are used, which consist of a combination of springs and dashpots both in series and parallel [11, 13].

The effect of viscoelasticity can be added to the model by adjusting the Young's modulus. The literature [24, 20] states that the Young's modulus in the Korteweg equation can be replaced by the complex Young's modulus $E^*(j\omega)$, resulting in a complex, frequency dependent wavespeed.

$$a(j\omega) = \sqrt{\frac{K}{\rho}\left(1 + \frac{DK}{eE^*(j\omega)}\right)^{-1}} \tag{2.35}$$

The pressure response from $x = 0$ to $x = 0.6$ is plotted in figure 2.7 for different damping ratios and Young's moduli. The geometry of the tube is the same as the one-section tube listed in table 2.1.

The top plot in figure 2.7 shows that having a higher loss tangent results in better damped resonance peaks and more decay at higher frequencies. The peaks and zeros remain at the same frequency. The bottom plot shows that using a more compliant tube is very effective for increasing the amount of damping imposed on the fluid even-though the loss modulus is lower. At higher frequencies, the resonance peaks are completely damped and the transfer function decays according to the following formula.

$$\lim_{f\to\infty} \frac{p_x}{p_i} = e^{-\frac{2\pi i x}{a(i\omega)} f} \tag{2.36}$$

When looking at the magnitude the following holds

$$\lim_{f\to\infty} \left|\frac{p_x}{p_i}\right| = e^{-\alpha f} \quad \text{with} \quad \alpha = \text{real}\left(\frac{2\pi i x}{a(i\omega)}\right) \tag{2.37}$$

meaning that the decay exponential α is linearly dependent on x, which is the tube length between the two sensors. This means that the tube length after x does not aid in adding more pressure decay at high frequencies.

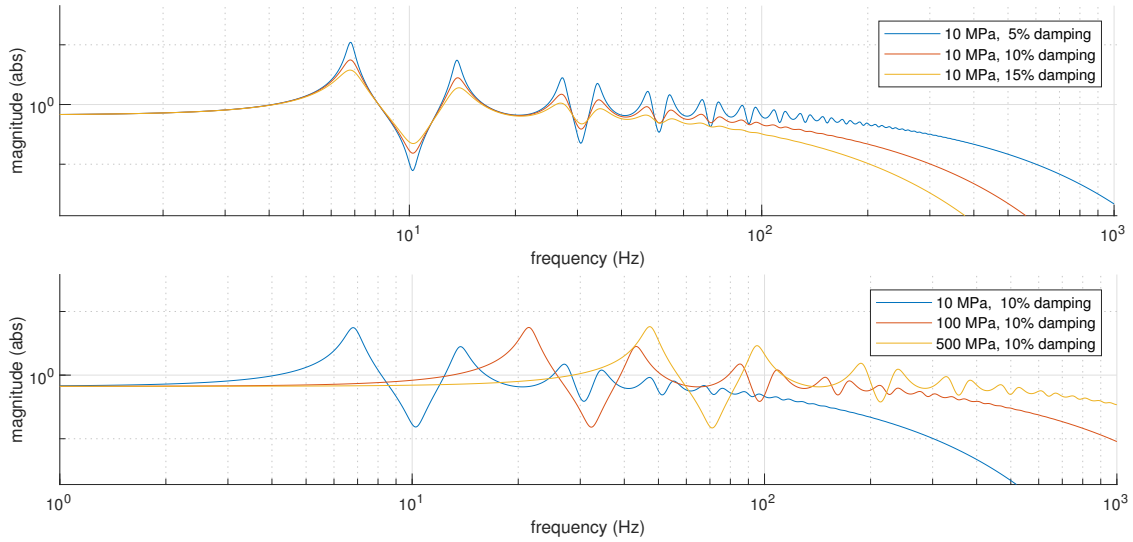

Figure 2.7: Pressure response for different damping ratios and Young's moduli. The use viscoelastic materials results in a pressure decay at high frequencies. The bottom plot shows that compliant materials are very efficient at attenuating pressure.

For a two section tube, the decay exponential can be expressed as

$$\alpha = \text{real}\left(\frac{2\pi i(l_{1x}-l_1)}{a_1(i\omega)} + \frac{2\pi i(l_{2x}-l_2)}{a_2(i\omega)}\right) \tag{2.38}$$

where $(l_{1x}-l_1)$ and $(l_{2x}-l_2)$ are the lengths of the respective tubes that lie in-between the probing points of the transfer function.

Figure 2.8 shows the frequency response for a steel tube with a viscoelastic tube before it. The properties of the steel tube are given in table 2.1. The the viscoelastic tube has the same length, diameter and wall thickness, but the Young's modulus is 550 MPa with 12% damping.

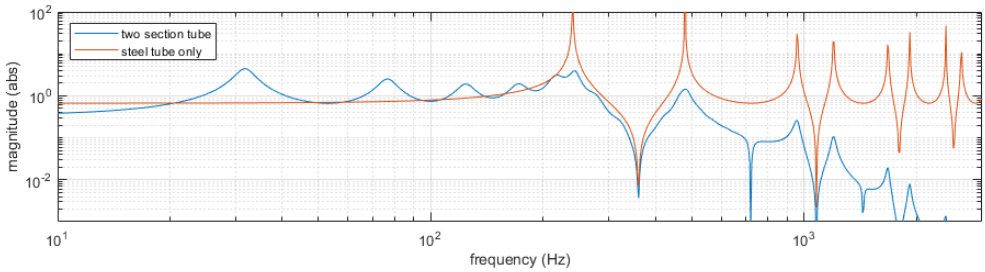

Figure 2.8: Frequency response function for a steel tube with and without a PTFE tube before it.

The resonances and anti-resonances from the steel tube can still be seen in the two-section model although the peaks are damped. The viscoelastic tube is responsible for the presence of the well-damped low frequency peaks, because the Young's modulus is around two orders of magnitude lower than the Young's modulus of steel.

2.6. Experimental validation

The theory behind the fluid dynamics in a liquid filled tube has been presented in the previous sections. This theory is well suited to model the fluid behaviour in viscoelastic links. The fluid resonance behaviour and pressure decay will be verified by means of an experiment. Measurements will be performed on three different viscoelastic tubes made from viton rubber, silicon rubber and PTFE (also known as Teflon). Based on the model and measurement results, the most suited material can be found.

2.6.1. Setup overview

A schematic representation of experimental setup is shown in figure 2.9. The setup consists of the following components:

- *Chiller*: a chiller is used to maintain flow in the circuit. The chiller consists of a small 1.3 liter reservoir, a pump and a heat exchanger. Fluid entering the chiller first flows into the reservoir.
- *Buffer reservoir*: an additional buffer reservoir with a higher capacity (~60L) has been placed before the chiller inlet, because the small reservoir alone created an additional pressure disturbance which propagates over the backside of the circuit
- *Flow regulator valves*: two valves are placed behind the chiller outlet. These are used to regulate the flow speed. The valve directly behind the outlet is used to restrict the flow exiting the chiller and the valve before the bypass is used to regulate the flow directly flowing back to the reservoir. A third valve is placed after the large buffer. This valve is left open during operation.
- *Flow sensor*: this sensor is placed after the flow regulator valves. The sensor measures the flow with a spinner wheel, which is rotated by the flowing medium. The measurement range of the sensor is 0.1 - 1.5 L/min
- *Viscoelastic tubing*: the viscoelastic tubes are placed behind the first and second pressure sensor. Measurements will be done with different tube materials. The tubes with an inner diameter of 6mm and an outer diameter of 8mm have been used throughout the fluid circuit
- *Pressure sensors*: two pressure sensors are used to measure the pressure at two points in the circuit. For this, the PCB 112A22 [18] has been selected. This sensor measures the pressure with a sensitive piezo element. It has been chosen based on it's high sensitivity and small diaphragm diameter. A manifold has been designed to integrate the sensor in the fluid circuit. The manifold features an intricate design to eliminate sharp edges inside the fluid duct. As a result turbulence will not be induced by the flowing fluid. Appendix D provides a detailed explanation of the manifold design.

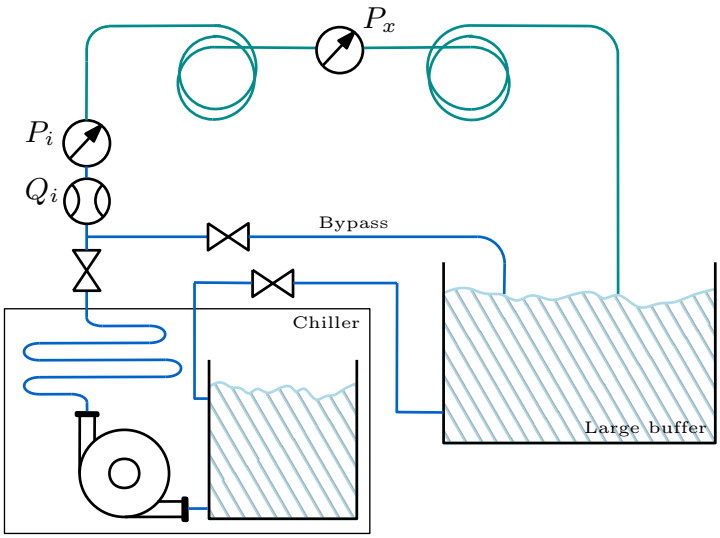

Figure 2.9: Schematic overview for the experimental setup. The chiller contains a small buffer reservoir, a pump and a heat exchanger. The valves behind the chiller are used to regulate the fluid flow. Two sensors are used to measure the flow and pressure behind the regulating valves. The viscoelastic tubes are marked with a different colour.

The flow sensor and the valves before the first pressure sensor will, besides the pump, also generate acoustic disturbances in the liquid. All components in front of the first pressure sensor will be generalized as a black box pressure disturbance source. The circuit behind the first sensor has been designed such that there are no sharp diameter changes or sharp edges within it.

The water at the end of the tube is freely flowing back above the large buffer. The tube is mounted above the water. This means that a zero pressure boundary condition can be enforced and that there will not by any

back pressure disturbances that propagate over the backside of the circuit. Earlier measurements have been performed without the large buffer. However, this caused excessive sloshing in the small buffer in the chiller, which caused the measurements to be inaccurate and unrepeatable.

An estimator is used to obtain the frequency response function (FRF) from the measurement data. The most common approach to the estimation of FRF's is by using the least squares method. Two popular least squares estimators are: the H1-estimator and the H2-estimator. Both algorithms can be used for time-invariant linear systems. The H1-estimator assumes that noise enters the system at the input and the H2-estimator assumes that the noise is entered at the output [21], see figure 2.10.

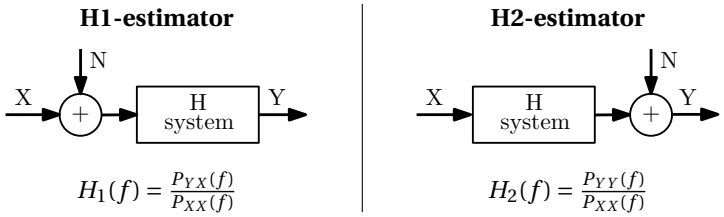

Figure 2.10: Comparison between an H1 and H2 estimator with P_{XX} and P_{YY} being the power spectral densities and P_{XY} being the cross power spectral density.

For this measurement, the signal power at the output will be lower compared to the input due to the viscoelastic tubing. Therefore, relatively more noise is expected to enter at the output and hence an H2-estimator is used. The coherence function gives the degree of causality between the system input and output. It is computed according to

$$C_{XY}(f) = \frac{\left|P_{XY}(f)\right|^2}{P_{XX}(f)P_{YY}(f)} \tag{2.39}$$

If the coherence equals one, the system is said to have perfect causality, meaning that output power is totally caused by the input power. The output power is greater than the input power if the coherence is less than unity. This is due to extraneous noise entering the system. The coherence is usually low at poles and zeros, which is often an indication of leakage since the FRF is most sensitive to leakage errors at minima or maxima [21].

2.6.2. Viton rubber tube

Rubber is known for its excellent damping characteristic. Specifically, viton rubber is used in vacuum applications, because it creates limited outgassing. The loss tangent of viton rubber is greater than the loss tangents of PTFE and silicone rubber and therefore the material should provide the most damping to the fluid. An experimental characterisation of a viton rubber was available for this research. A tenth order generalised Maxwell fit of rubber behaviour is plotted in figure 2.11.

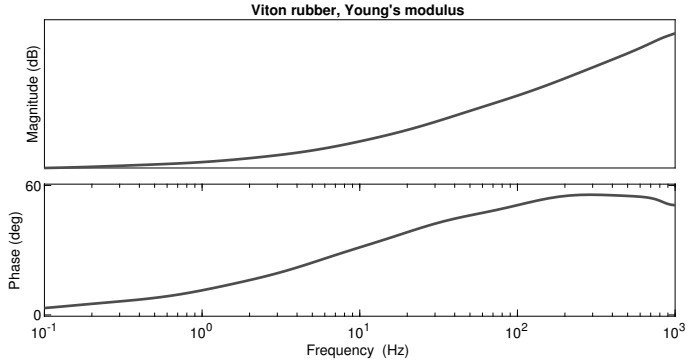

Figure 2.11: Tenth order Maxwell model from the Young's modulus of a viton rubber. The axis values are hidden for confidentiality reasons.

It shows the magnitude and the phase of the dynamic Young's modulus over frequency. The axis values are

partly hidden for confidentiality reasons. It can be noted that the Young's modulus increases over frequency meaning that the fluid speed of sound rises as well according to equation 2.35.

A schematic overview of the fluid circuit with a viton rubber tube is shown in figure 2.12a. The tube has a total length of 4.4 meter and the second pressure sensor has been placed at x = 2.2m. The frequency response function between the pressure at p_i and p_x is shown in figure 2.12b. The modelled frequency response is shown for two different support conditions, one where the tube is free to move axially and one where the tube is anchored throughout its length.

The experimental results and the model of the second support condition show good agreement up to approximately 50Hz. The tube has been placed on the ground during the experiment and therefore the support condition is not very well defined. One could argue that the tube is anchored throughout, since the small axial forces are likely not great enough to overcome static friction.

(a) Schematic overview of the setup

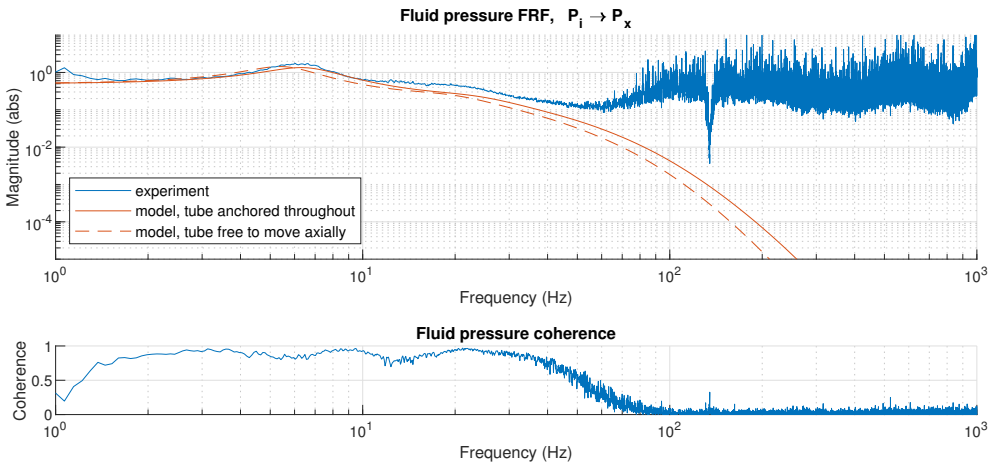

(b) Measured and modelled frequency response function from P_i to P_x. The modelling results are presented for two different support conditions.

Figure 2.12: Fluid transient behaviour of water conveyed through a viton rubber tube.

2.6.3. Silicon rubber tube

Silicon rubber is more compliant than viton rubber. The Young's modulus of the material is 3.6MPa, which has been derived based on the hardness given by the manufacturer. The loss tangent is found to be 0.12 [30, 29]. A schematic overview of the fluid circuit with a silicon rubber tube is shown in figure 2.13a. The tube has a total length of 4.4 meter and the second pressure sensor has been placed at x = 2.2m. The frequency response between both pressure sensors is shown in figure 2.13b. The model has been made with the assumption that the tube is anchored throughout.

The result shows that the resonances between the model and experimental results are shifted. This is most likely caused by the static Young's modulus that has been used in the model, while in fact the Young's modulus is frequency dependent and rises with frequency. This behaviour was also observed in the material model of viton rubber. Therefore, the Young's modulus at the first frequency peak will be higher than actually modelled, resulting in a peak that is shifted to the left. The frequency shift can also be explained by the uncertainty in the Young's modulus. The material properties of polymers are highly temperature dependent and the properties may differ per manufacturer or even per production batch. A second model with higher Young's modulus is also shown in the figure. The Young's modulus has been fitted such that the first frequency peak intersects. This model shows that the peaks start to drift again at higher frequencies. A better model can be made by measuring the dynamic material behaviour and implementing the results into the model. Note that there are no anti-resonances present in the model since the resonances and anti-resonances cancel according to equations 2.24 and 2.25 because the sensor is placed exactly in the middle. However, in practice it can be observed that is not exactly the the case: the experimental results show a peak at 7.2Hz. Lastly, it can be seen

(a) Schematic overview of the setup

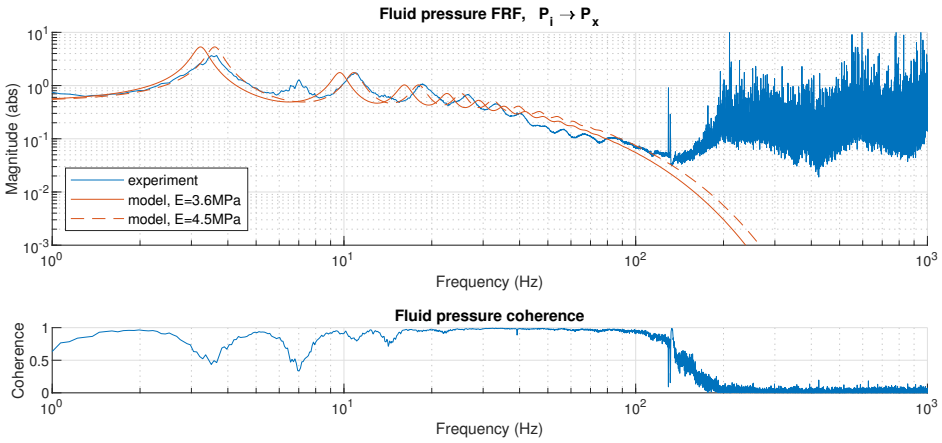

(b) Measured and modelled frequency response function from P_i to P_x. The modelling results are presented for two different Young's modulus values.

Figure 2.13: Fluid transient behaviour of water conveyed through a silicon rubber tube.

that the coherence drops at the frequency peaks. This is often an indication of leakage since the frequency response function is most sensitive to a leakage error at lightly damped peaks corresponding to the maxima.

2.6.4. PTFE tube

PTFE is a synthetic fluorpolymer, also known by the brand name Teflon. The material is significantly stiffer than rubber and silicon. The Young's modulus of the PTFE tube is 550MPa according to the specsheet of the manufacturer and the loss tangent of PTFE is found to be 0.12 [26]. A schematic overview of the fluid circuit with PTFE tubes is shown in figure 2.14a. A longer tube has been used to bring the first eigenfrequency down for better measurement results. The tube has a total length of 11 meter and the second pressure sensor has been placed at x = 7m. The frequency response between both pressure sensors is shown in figure 2.14. The model assumes that the tube is anchored throughout.

(a) Schematic overview of the setup

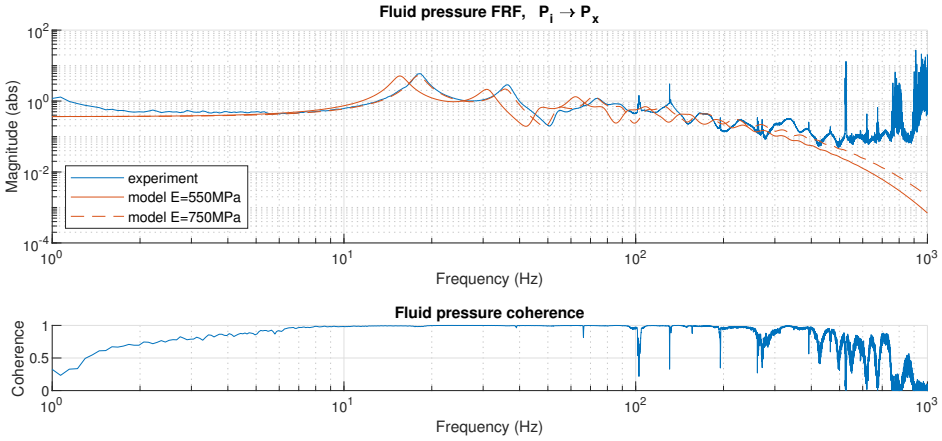

(b) Measured and modelled frequency response function from P_i to P_x. The modelling results are presented for two different Young's modulus values.

Figure 2.14: Fluid transient behaviour of water conveyed through a PTFE tube.

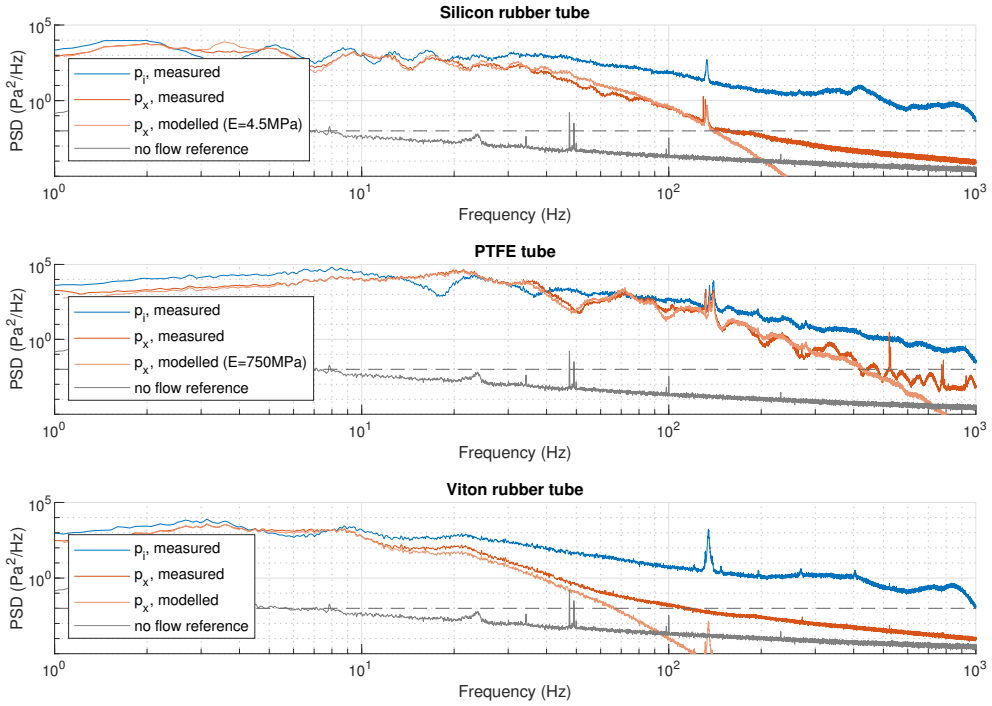

Figure 2.15: PSD of the fluid pressure at the second sensor. Results are shown for a silicon rubber, PTFE and viton rubber tube. The modelled and experimental results start to deviate once the signal drops below 1×10^{-2} Pa^2/Hz. This value is marked by the dashed line.

The results show that the resonances between the model and the experimental results are shifted. This is most likely explained by the use of a static Young's modulus and by the uncertainty in material properties. A second model with higher Young's modulus is also shown. A better model can be made by measuring the dynamic material behaviour and implementing the results into the model.

The results show that viton rubber provides the most damping out of the tested materials. At 40Hz, viton rubber provides a pressure reduction of a factor 6.7 while silicon only achieves a reduction factor of 3.3. The pressure decay of PTFE is also worse than rubber, even-tough the tube in the experiment is significantly longer.

2.6.5. Model limitations

The previous results show good agreement between the model and the experiment. However, from a certain frequency the experimental results only show noise and the coherence drops to zero. This would suggest the presence of another disturbance source that enters the system at another point. Figure 2.15 shows power spectral density plots of the measured pressures p_i and p_x for the three different tubes. Furthermore, it shows the modelled pressure at p_x based on p_i, calculated according to

$$PSD_{p_x}(f) = \left|G_{p_i \to p_x}(f)\right|^2 \cdot PSD_{p_i}(f) \tag{2.40}$$

All graphs show that the measured and modelled pressure for p_x start to deviate once the signal drops below around 1×10^{-2} Pa^2/Hz. This happens at 105 Hz for the silicon tube, at 400 Hz for the PTFE tube and at around 80 Hz for the rubber tube. These are also the regions where the coherence between p_i and p_x drops.

A possible reason for this limitation in the model can be additional flow induced disturbances generated around the second pressure sensor (p_x). Despite great efforts to eliminate sharp edged in the circuit, small irregularities that generate disturbances can still be present. For example, the pressure sensor is not perfectly flush with the manifold (see appendix D). Furthermore, a small metal insert is placed at the ends of the viscoelastic tubing in order to be able to use a clamp coupling around it. Both of these irregularities can contribute to the unpredictable high-frequency behaviour.

3

Acoustic-structure interaction in liquid filled tubes

The disturbances generated in the cooling conduit are caused by the interaction between the pressure pulsations in the fluid and the mechanics of the cooling conduit. This section covers this interaction mechanism. A finite element model is devised that is able to predict the resulting reaction force on the conduit due to a fluid pressure excitation.

The chapter is structured as follows. The first section describes the tube excitation mechanisms, explaining how pressure pulsations produce a resultant force on the tube. Section 3.2 elaborates on the influence of mechanical vibrations of the tube on the fluid pressure. The setup of the finite element model is covered in section 3.3. Two models with and without bidirectional coupling are discussed in section 3.4. Finally, the chapter is concluded with a measurement, which is conducted to validate the fluid-structure interaction model.

3.1. Tube excitation mechanisms

The pressure pulsations in the fluid will apply a force on the tube boundary, causing it to accelerate. The force per unit area applied on the tube wall ($\mathbf{F}_A$) is given by

$$\mathbf{F}_A = p\mathbf{n} \tag{3.1}$$

with p being the fluid pressure and $\mathbf{n}$ the normal of the tube wall. The pressure force on the tube will result in a circumferential stress in the tube, also know as hoop stress. A radial expansion of the tube results in an axial compression due to the Poisson effect. Applying an oscillating pressure at the input will therefore excite the axial modes of a tube. This is the only fluid excitation mechanism for tubes without bends. However, this effect will usually be negligible.

For curved tubes there will be another mechanism that excites the tube. An example of a curved tube is shown in figure 3.1a. The plot shows the pressure load at the tube wall. Note that the wall area at the right side of the bend is larger than the area at the left side. As a consequence, the fluid load $\mathbf{F}_A$ will act over a bigger area on the right side, causing a resultant fluid load over the curved section, pointing outwards. The resultant fluid load $\mathbf{f}_l$ for a tube with a circular cross-section can be calculated according to

$$\mathbf{f}_L = -pA_f\kappa\mathbf{n} \tag{3.2}$$

with p being the fluid pressure, A_f the fluid cross-sectional area, κ the curvature of the tube centreline and $\mathbf{n}$ the normal of the centreline. This formula is proven in appendix E.

Now lets consider the fluid conduit from the experimental setup. The geometry is shown in figure 3.2. The conduit consists of two 180-degree bends in the xy-plane and two 90-degree bends, which are out-of-plane. The tube is made of steel. It has a 6mm inner diameter and a wall thickness of 1mm. The conduit is fixed at three positions and has a total length of 2.29 m.

Five fluid couplings are placed in the circuit. These are often used in cooling circuits for easy assembly and disassembly. The couplings will add mass, altering the dynamics of the tube. Therefore it is important to take them into account in the model.

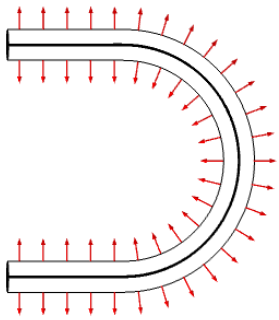

(a) Fluid load on the wall (in N/m^2) calculated according to equation 3.1

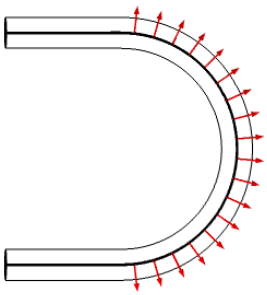

(b) Result fluid load (in N/m) defined on the centreline of the tube according to equation 3.2

Figure 3.1: Wall pressure and resultant fluid load on a bend tube. The tube has a straight section, a 180 degree bend and again a straight section. The fluid has a uniform pressure amplitude of 1Pa

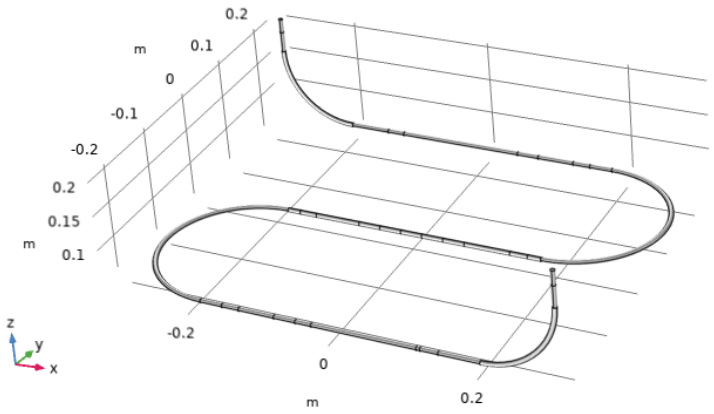

Figure 3.2: Geomtry of the fluid conduit. The total length of the tube is 2.29 m

The pressure amplitude at the tube input is prescribed to be 1 Pa and the pressure at the output is 0 Pa. The pressure along the axis of the tube will drop linearly from 1 Pa to 0 Pa at low frequencies as described in section 2.3. The pressure distribution and the resulting fluid load are shown in figure 3.3. The load on the tube is countered by the tube supports. For this example a 1Pa input pressure will result in a reaction force of 2.98×10^{-5} N. Note that the reaction force is not constant over time, but oscillates with the input pressure. The force amplitude is dependent on the number of bends in the conduit and the cross-sectional area of the tube. Adding more bends and increasing the cross-sectional area will increase the reaction force magnitude.

3.2. Bi-directional coupling

Formula 3.1 only takes the acoustic pressure acting on the tube into account. However, the converse, where the vibrating structure causes sound to be generated in the fluid should also be considered. This mechanism is significant if a structure is radiating into a heavier-than-air medium such as water, or if a structure is very lightweight, such as with a thin walled tube. The fluid pressure response of a vibrating tube is governed by the following equation

$$\mathbf{n} \cdot \left(\frac{\nabla p}{\rho} \right) = -\mathbf{n} \cdot \mathbf{u}_{tt} \tag{3.3}$$

where $\mathbf{u}_{tt}$ is the structural acceleration of the tube, $\mathbf{n}$ is the surface normal and p is the acoustic pressure. The fluid acceleration perpendicular to the tube will be equal to the perpendicular tube acceleration. This will generate a pressure gradient. Therefore, the formula states that an acceleration perpendicular to the tube wall will result in a radial pressure gradient inside the tube. The bi-directional fluid coupling can be taken into account by evaluating formula 3.1 and 3.3 at inner the boundary of the tube. The influence of bi-directional coupling on the fluid pressure is illustrated with an example in section 3.4.

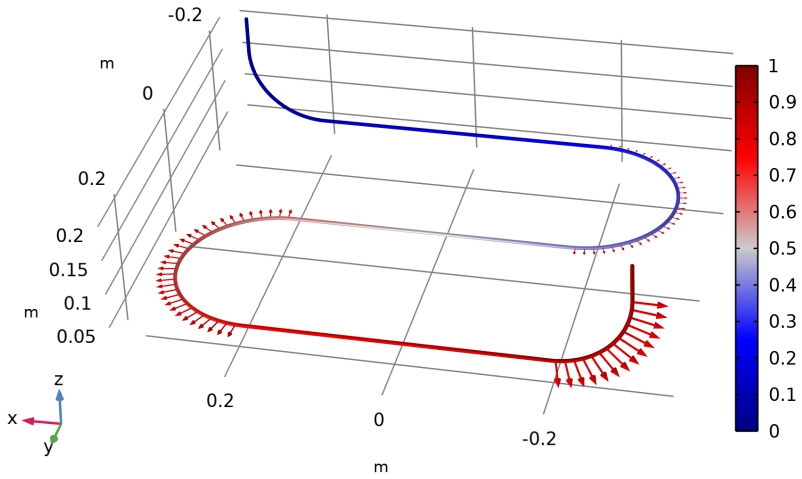

Figure 3.3: Fluid load at 1Hz on the conduit described in section 3.1. The applied pressure amplitude at the input is 1Pa and the pressure at the output is zero. The fluid load direction and magnitude is given by the arrows and the pressure distribution is shown by the colour scale. The values are in Pascal.

3.3. Model construction

The final model will be solved by using the finite element method (FEM). A software package called COMSOL Multihysics has been used to perform the calculations because this software well known for its excellent multi-physics capabilities. FEM calculations generally require more computing power, compared to other solution methods. However, the method has several advantages. Today's FEM software packages make it is easy to link subcomponents with different physics interfaces, which are in this case the tube and the fluid contained in the tube. Besides this, it is convenient to load in the geometry of the cooling conduit together with the support locations. The entire model has been implemented in 3D space. The tube has been modelled using shell elements and the fluid is modelled with pressure acoustic elements. The mechanics of the plate are not taken into account in this model, therefore the supports are considered to be rigid. The fluid couplings and pressure sensor manifold, have been modelled by adding mass to the surface of the shell elements.

The pressure acoustic elements have been defined using the following relation

$$\frac{\partial \mathbf{u}}{\partial t} + (\mathbf{u}\cdot\nabla)\mathbf{u} = -\frac{1}{\rho}\nabla p \tag{3.4}$$

$$\frac{\partial \rho}{\partial t} + \nabla\cdot(\rho\mathbf{u}) = 0 \tag{3.5}$$

This equation models the fluid assuming compressible lossless flow. The 3 dimensional approach allows us to model tube deformations with non-rigid cross-sections and non-planar fluid responses. This is however only necessary for high-frequency modelling.

An important aspect to consider while building a finite element model is the mesh density. The selection of an insufficient mesh density may lead to inaccurate or incorrect results, while the selection of an excessive mesh density can cause unnecessarily long computation times. For an acoustic analysis, the recommended mesh density is dependent on the number of elements per wave wavelength. This, in turn, is dependent on the element order of the shape function. The model uses a second-order discretization and therefore it is required to have 5 to 6 elements per wavelength. Second-order elements are chosen because they generally represent a good compromise between accuracy and computational requirements.

The acoustic wave speed in the steel tube can be calculated according to formula 2.35, resulting in a wavelength of 1.44 m at a frequency of 1000Hz. This would only require 5 or 6 elements for the conduit. However more elements were chosen to resolve the geometry correctly.

The mesh of the model is shown in figure 3.4. The mesh consists of triangular prismatic elements (see figure 3.5). These elements feature 6 nodes and can have a high aspect ratio, whereas commonly used tetrahedra elements generally have an aspect ratio close to unity. Using prismatic elements enables us to have stretched elements along the length of the tube.

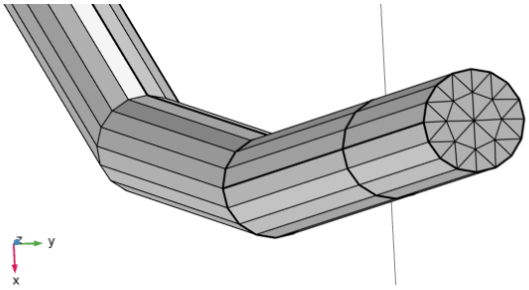

Figure 3.4: Model mesh. Shell elements are used at the tube wall and pressure acoustic elements are used inside the tube.

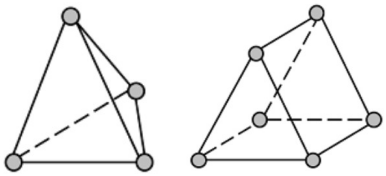

Figure 3.5: Schematic representation of a tetrahedra and triangular prismatic element

For this research we are interested in the frequency response of the system therefore a harmonic analysis will be performed. This analysis is used to calculate the acoustic or vibration response of a system due to excitation by a sinusoidally varying driving force, in this case the inlet pressure. The equations of motion for an acoustic or structural system can be written as

$$\left(-\omega^2[\mathbf{M}] + j\omega[\mathbf{C}] + [\mathbf{K}]\right)\{\mathbf{u}\} = \{\mathbf{f}\} \tag{3.6}$$

where [**M**] is the mass matrix, [**C**] the damping matrix, [**K**] the stiffness matrix, {**u**} the nodal displacements and {**f**} the applied load. The frequency behaviour can be computated by inverting the combined mass, stiffness and damping matrix according to the following equation for a sweep of frequencies.

$$\{\mathbf{u}\} = \left(-\omega^2[\mathbf{M}] + j\omega[\mathbf{C}] + [\mathbf{K}]\right)^{-1}\{\mathbf{f}\} \tag{3.7}$$

This process is computationally expensive since the matrix inversion needs to be performed at every frequency sample. The model used here takes a logarithmic frequency sweep over a frequency range from 1 to 1000Hz. The sweep has been refined around the resonance peaks of the model in order to better capture the behaviour at the frequency peaks and save on computation time. A detailed overview of the model setup can be found in appendix G.

3.4. One-directional coupling versus bi-directional coupling

Two different models have been considered: a model with a one-directional coupling and a bi-directional coupling. The one-directional model only takes into account the acoustic pressure acting on the tube, according to equation 3.2, whereas the two-way model takes the bi-directional coupling into account.

In the one-directional model, the pressure load is applied on the shell as a boundary condition. A segregated solver is used to solve the model, meaning that the model is subdivided in multiple steps. The solver first solves for the pressure by only considering the acoustic elements. The displacements of the tube are computed in the second step. The system matrices for both solving steps are symmetric.

A fully coupled solver is used to resolve the two-way model. This model considers both the pressure acoustics and the shell mechanics at the same time. The pressure acoustics and shell mechanics are coupled at the boundary governed by equations 3.2 and 3.3.

The fully coupled approach forms a single large system of equations that solves for all of the unknowns. The system matrix is nonsymmetric due to the off-diagonal coupling terms. Solving nonsymmetric matrices requires more computational resources compared to solving a symmetric matrix

Both the one-directional and bi-directional model will be used to compute the pressure distribution and reaction force of the fluid conduit from the experimental setup shown in figure 3.2 to asses the difference between both models. An oscillating pressure of 1Pa is applied at the input and the pressure at the output is prescribed to be 0Pa. Two transfer function are plotted in figure 3.6. The first transfer function shows the fluid pressure at the output of the conduit P_2 as a result of the driving pressure applied at the input P_1, while the second transfer function shows the total reaction force on the tube supports as a result of the same driving pressure P_1. Both the one-directional and bi-directional models are linear, meaning that increasing the excitation pressure by a factor 2 will also increase the reaction force by the same factor. This means that the solver only needs one Newton-Rapson iteration to arrive at the solution.

The pressure transfer of the one-directional model clearly shows fluid resonances at 324, 648 and 972Hz. This model is the same as one would get when using the analytical pressure transfer function for a rigid tube

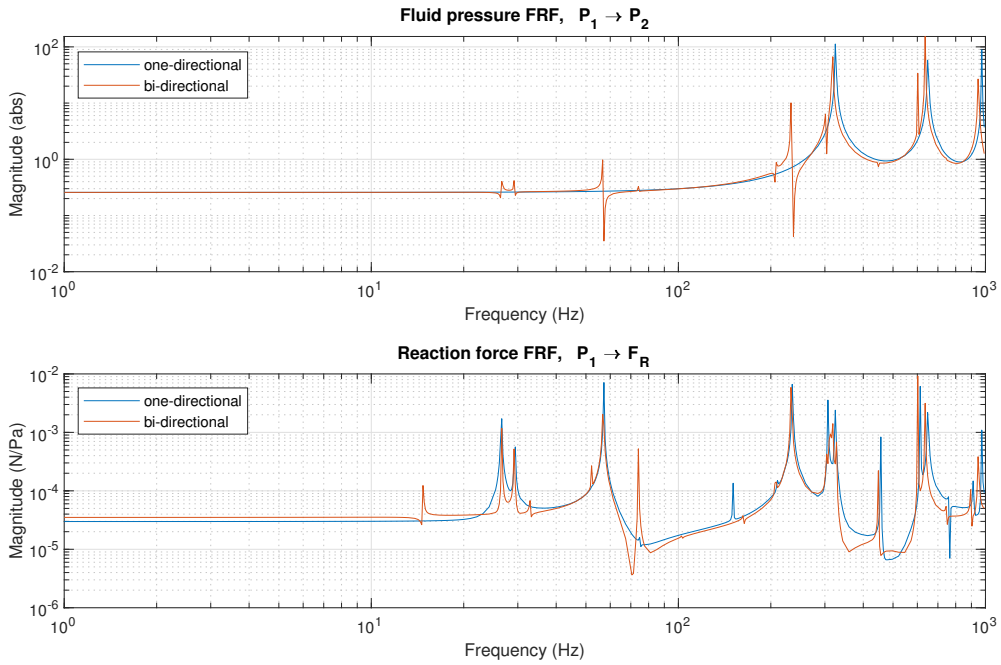

Figure 3.6: Modelled transfer functions of the output pressure p_2 and the reaction force F_R. Both transfers are taken from the input pressure p_1. The result for the one-directional and bi-directional model are both shown.

(see equation 2.22). However, the bi-directional model shows that the fluid pressure is also influenced by the dynamics of the tube. Additional peaks are observed at the eigenfrequencies of the tube. Here, the motion of the structure influences the fluid pressure resulting in non-axial pressure waves. The first four eigenmodes of the tube are plotted in figure 3.7.

The reaction force of the one-directional and bi-directional model roughly show the same behaviour. However, the bi-directional model shows additional resonances. The mechanical modes of the tube at 15.0, 33.5 and 75Hz are not excited in the one-directional model, but they are in the bi-directional model. Furthermore, the one-directional model predicts a constant 2.98×10^{-5} N reaction force before the first frequency peak. This is the reaction force needed to counteract the fluid load as a result of the linear pressure drop, shown in figure 3.3. The magnitude of this force depends on the cross-sectional area of the tube and the number of bends. Below the first resonance, the reaction force predicted by the bi-directional model is slightly higher. The reason for this is unknown.

3.5. Experimental validation

A setup has been devised to verify the one-directional and bi-directional coupling mechanisms. The setup is shown in figure 3.8 and 3.9. It, again, consists of a 2.29 m long steel tube, however the 90-degree bends at the in- and outlet are rotated compared to the previous model. The pressure is measured before and after the conduit. A 4m long PTFE tube is connected to the output of the conduit to transport the fluid to a buffer reservoir. Furthermore, the tube vibrations are measured by an accelerometer that is positioned in the middle of the conduit.

The viscoelastic PTFE tube will induce damping on the pressure resonance peaks, as explained in section 2.5. For this reason, the 4m PTFE tube is also included in both the one-directional and bi-directional models. The plate is assumed to be rigid and therefore the dynamics of the plate are not modelled. This assumption can be made for frequencies below the first eigenmode of the plate, which occurs at 260Hz.

Two transfer functions are plotted in figure 3.10. The first transfer function shows the fluid pressure at the end of the steel conduit as a result of the driving pressure at the input. The second transfer function shows the structural tube acceleration measured at the accelerometer as a result of the same driving pressure. This transfer function is useful to investigate the excited eigenmodes and their influence on the fluid pressure. The experimental transfer function has been computed by measuring the pressure before and after the plate

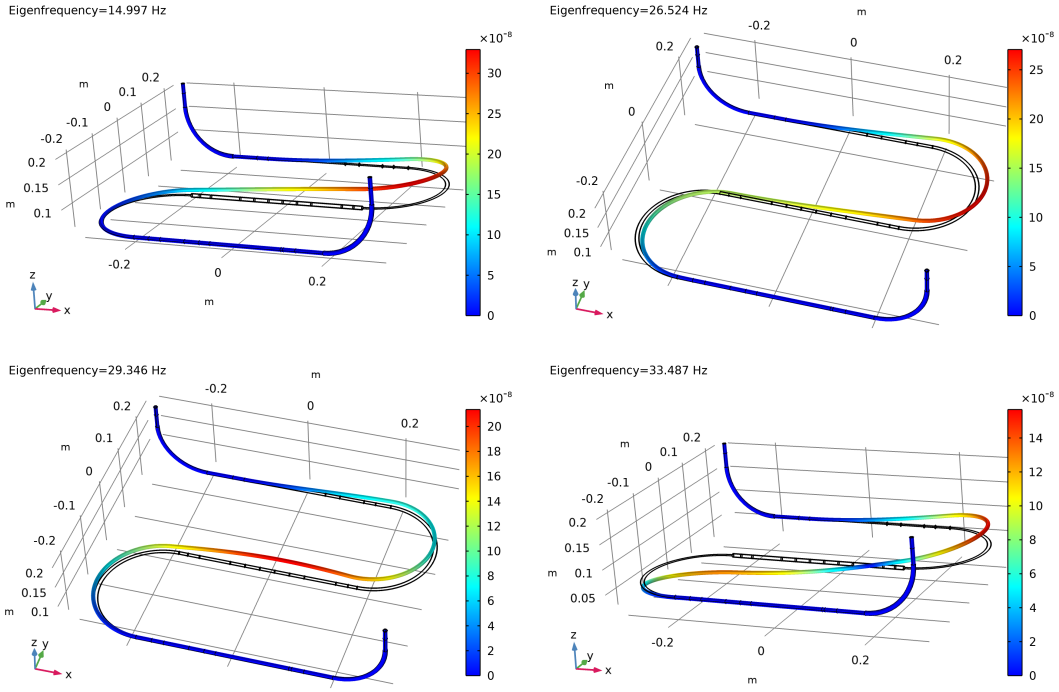

Figure 3.7: Deformation plot of the first 4 eigenfrequencies in meters. The 15.0 and 33.5 Hz eigenmodes show deformations in the z-direction while the 26.5 and 29.3 Hz modes show deformations in the xy-plane.

and by using an H2-estimator (see figure 2.10).

The experimental results clearly show that the structural acceleration of the tube has an influence on the fluid pressure, as was also predicted by the two-way model. Small pressure ripples can be observed at the eigenfrequencies of the tube. This is apparent at 15.0 Hz, 28.3 Hz, 86.7 Hz and 189.1 Hz. These frequencies coincide with the tube resonances measured by the accelerometer

The measured and modelled acceleration functions show good resemblance. The experimental results show a lot of resonances between 40 and 200Hz. These are likely caused by vibrations from the ground. The setup can be improved upon by placing the plate on a heavy block of granite with vibration isolation. Note that the model is not fully representable above 260Hz which is the first resonance frequency of the plate.

The one-directional model computes the solution around 40% faster and uses less memory. However, it chosen to use the two-model because accuracy is preferred over the limited improvement in computation time.

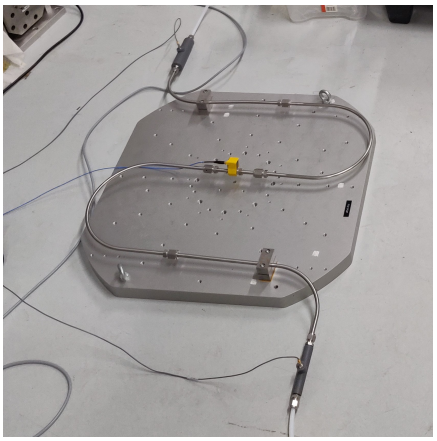

Figure 3.8: Picture of the experimental setup. The tube is fixed at two locations and the pressure is measured at both the in- and outlet. Furthermore, an accelerometer is mounted in the middle of the conduit.

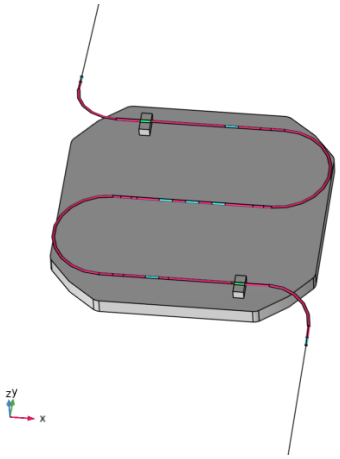

Figure 3.9: Model of the experimental setup. The fluid couplings are included by adding mass to the tube walls marked light blue

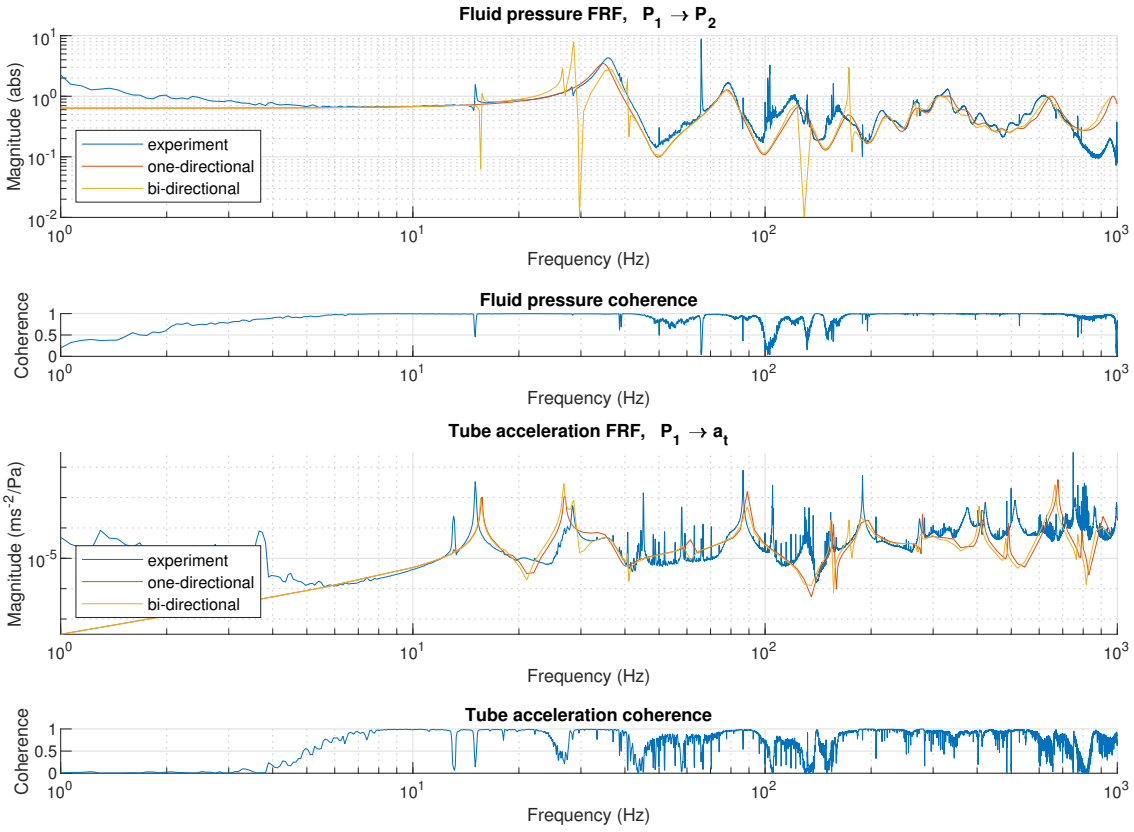

Figure 3.10: Transfer functions of the output pressure p_2 and the tube acceleration a_t. Both transfers are taken from the input pressure p_1. The experimental results are shown together with the one-directional and bi-directional model results.

4

Transmission of pump induced vibrations in a mechatronic application

The tools required to model the transmission of pump induced vibrations to a precision system have been provided in chapter 2 and 3. The fluid dynamics in a viscoelastic dynamic link were discussed in chapter 2 and the fluid-structure in cooling conduits was covered in chapter 3. In this chapter, an experimental setup will be considered to verify the performance of the model in a mechatronic application. The setup, introduced in the introduction, is a representation of a simplified precision system. It has been designed mitigate external disturbances such as floor vibrations or acoustic noise in the environment. The system acceleration will be used as the performance measure for the disturbance magnitude.

This chapter is structured as follows. Section 4.1 gives a detailed overview of the experimental setup. The background disturbances measured on the plate are discussed in section 4.2. Section 4.3 discusses the finite element model used to predict the system acceleration. The measured and modelled accelerations are compared in section 4.4. Lastly, the influence of adding more supports or more viscoelastic tubes is investigated in section 4.5.

4.1. Setup overview

A setup has been devised in order to measure the magnitude and spectral behaviour disturbances generated by pump induced vibrations. The setup consists of a 20kg plate that is suspended from the ceiling by 4 elastic ropes. A steel cooling conduit is mounted on the plate with 3 supports. Pressure disturbances in the cooling fluid will result in small vibrations of the plate, which will be measured by two accelerometers.

4.1.1. Fluid circuit

A schematic representation of the fluid circuit is given in figure 4.1. The fluid conduit on the plate is connected with flexible tubes to the pump and fluid reservoir. These flexible links serve two purposes: to create a compliant coupling to the plate and the fixed world and to damp-out pressure pulsations from the pump. This is in accordance with a mechanically isolated, cooled structure in high-precision machines. The fluid flows back into a big buffer reservoir before re-entering the pump to prevent pressure disturbances from entering on the outlet of the circuit.

Two pressure sensors are mounted within the circuit: one behind the outlet of the pump and one in the fluid conduit on the plate. Furthermore, a flow sensor has been positioned behind the pump outlet. A fluid manifold has been designed to integrate the sensor in the circuit. The manifold features a smooth organic inner geometry, meaning that there are no sharp edges that can potentially create FIV, see appendix D for a more detailed explanation.

The fluid conduit on the plate consists of an S-shaped stainless steel duct that is supported with three mounts on the plate. Five VCR couplings are located in the circuit, because this makes the conduit to be a better reflection of a typical cooling conduit. The couplings will influence the eigenfrequencies of the system due to their added mass. It is important that the flexible links do not add stiffness to the connection between the plate and the fixed world. Therefore they should hang downward from the plate in an arc. The conduit has been mounted underneath the plate to achieve this.

The inner and outer diameters of all the tubes in the circuit are respectively 6 and 8mm. The setup has been made such that there are no diameter changes present within the circuit. This prevents FIV from being created at other locations besides the pump.

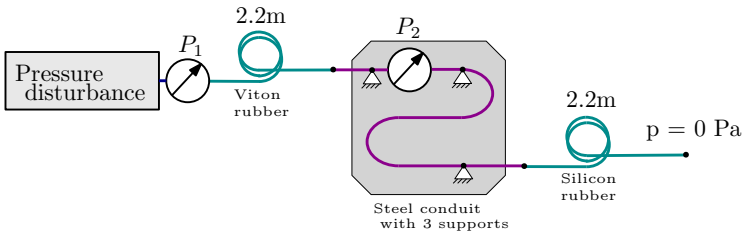

Figure 4.1: Schematic overview of the fluid circuit

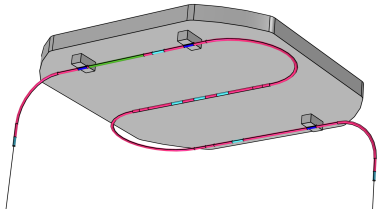

Figure 4.2: Fluid conduit with 3 supports. The light blue parts of the tube mark the locations of the fluid couplings and the green section marks the location of the pressure sensor manifold.

4.1.2. Plate dynamics

The first eigenfrequencies of the plate occur at 260Hz (saddle), 350Hz (saddle) and 410Hz (umbrella). Meaning that the plate acts as a rigid body up to 230Hz. Below this frequency, disturbance forces induced by the fluid can be calculated using Newton's second law, $F_{\text{disturbance}} = m_{\text{plate}} \cdot a_{\text{plate}}$. Two 1-DOF accelerometers are used to measure the acceleration of the plate. One sensor is mounted planar to the plate in the x-direction and the other is mounted perpendicular to the plate in the z-direction. A bracket is used to mount the accelerometers. The first eigenfrequency of the bracket with sensor mass occurs at 1362Hz, meaning that the mechanics of the bracket will not interfere below this frequency. The accelerometers are each connected to an amplifier and both amplifiers are connected to a data acquisition device. The amplifiers have been placed on top of the plate. The wires running from the plate to the fixed world can potentially transmit vibrations. Therefore these wires should be as flexible as possible.

4.1.3. Vibration isolation

The plate is suspended by four 2.8 m long elastic ropes in order to attenuate the vibrations from the ceiling. The relation between the vibrations on the ceiling and on the plate can be described by the transmissibility function.

$$\frac{x_p}{x_c} = \frac{2\zeta\frac{s}{\omega_0}+1}{\frac{s^2}{\omega_0^2}+2\zeta\frac{s}{\omega_0}+1} \tag{4.1}$$

where x_p and x_c respectively are the excitation of the plate and the ceiling, ζ is the damping factor and ω_0 is the eigenfrequency. The transmissibility has been measured by placing an additional accelerometer on the ceiling, measuring in the vertical direction. The result is shown in figure 4.3.

The figure shows a resonance peak that is not well damped. The resonance frequency and the damping ratio are respectively 1.1 Hz and 0.02. An ideal transmissibility function with these values is shown in the same figure. The combined stiffness of the four ropes (k) is

$$\begin{aligned} k &= 4\pi^2 f_0^2 m \\ &= 4\pi^2 \cdot (1.1\,\text{Hz})^2 \cdot 23.4\,\text{kg} = 1.12\times 10^3\,\text{N/m} \end{aligned} \tag{4.2}$$

At 3.6 Hz, the vibration isolation already attenuates the ceiling vibrations by a factor 10. This shows that ceiling vibrations will only contribute to the error at low frequencies ($f < 4$ Hz). The coherence starts dropping off after 12 Hz meaning that other disturbances sources, such as acoustic coupling are more dominant.

The pendulum frequency can be calculated according to

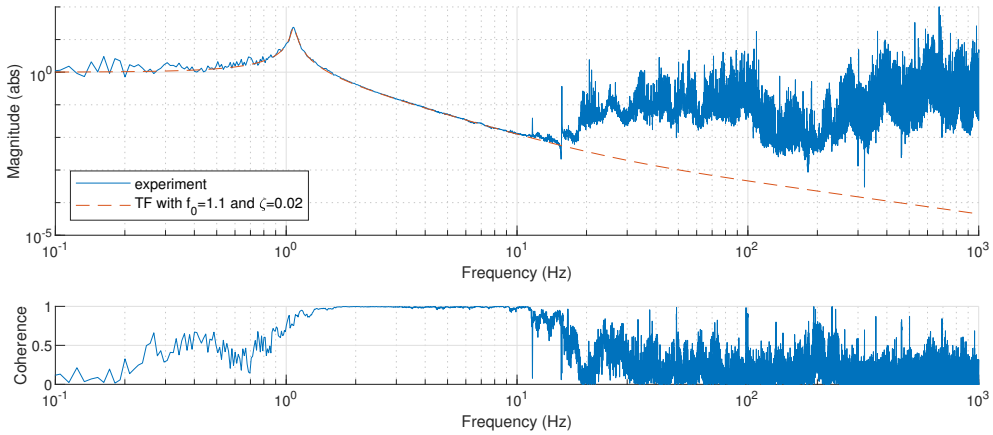

Figure 4.3: Transmissibility of vibrations between the ceiling and the floor in z-direction

$$
\begin{aligned}
f_0 &= \frac{1}{2\pi}\sqrt{\frac{g}{l}} \\
&= \frac{1}{2\pi}\sqrt{\frac{9.81\,\mathrm{m/s^2}}{2.8\,\mathrm{m}}} = 0.3\,\mathrm{Hz}
\end{aligned}
\tag{4.3}
$$

4.1.4. Acoustic disturbances

The main disturbance source on the plate is caused by acoustics. The plate is, therefore, placed inside an acoustic enclosure. The enclosure does not touch the plate, ropes or fluid conduit at any location, meaning that the plate is completely free to move. The enclosure has an inner wall of 18mm thick MDA plate, 100mm thick stonewool insulation material, 18mm MDA plate and 10mm plasterboard. Measurements and sound transmission loss theory show that adding more mass to the enclosure wall helps in improving its performance. Appendix F discusses sound transmission loss theory and the different iterations that have been made to the enclosure.

Figure 4.4: Picture of the setup with the lid of the acoustic enclosure open

Figure 4.5: Picture of the setup with the lid of the acoustic enclosure closed

4.2. Disturbance spectrum

Measurements have been performed on the setup with and without flow in order to determine the frequency ranges over which the pump disturbances is dominant. The measurement without flow has been performed with the dynamic links disconnected, but with the pump on, because the sound the pump produces should be taken into account to make a fair comparison. The measurement results are shown in figure 4.6.

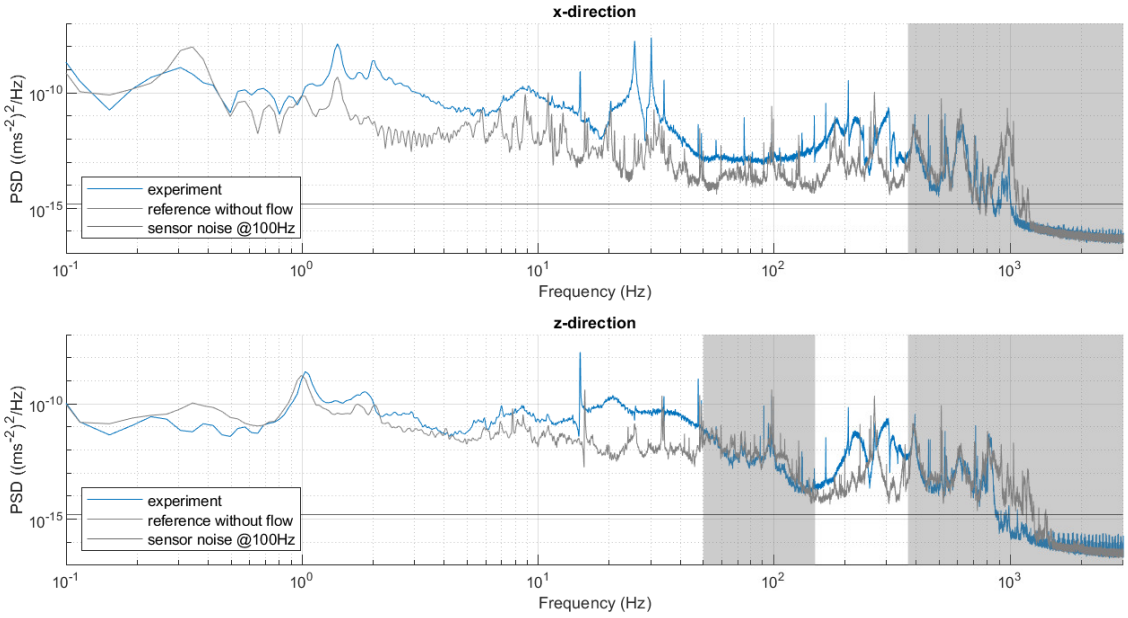

Figure 4.6: Power spectral density of the plate acceleration with the fluid circuit connected and disconnected. The pump is switched on in both measurements to ensure the same background conditions. The grey areas mark the frequency regions at which background disturbances are dominant.

The low frequency behaviour is predominantly caused by the suspension modes of the plate The resonance peak at 1.1Hz in the z-direction due to the elasticity of the ropes can clearly been seen. The acceleration in the x-direction shows suspension modes at 0.3Hz and 1.5Hz of which the 0.3Hz peak can be attributed to the pendulum frequency.

The grey areas in the figure mark the frequency ranges at which background disturbances are more dominant than disturbances generated by the fluid. The amplifier of the accelerometer has a low pass filter with a -3dB cut-off at 450Hz. Above 1500Hz the data is only showing electrical noise from the data acquisition device

The PSD plot of the pressure disturbance produced by the pump is shown in figure 4.7. The pressure spectrum can roughly be described by a low-pass filter. The root-mean square pressure is calculated to be 934.8 Pa.

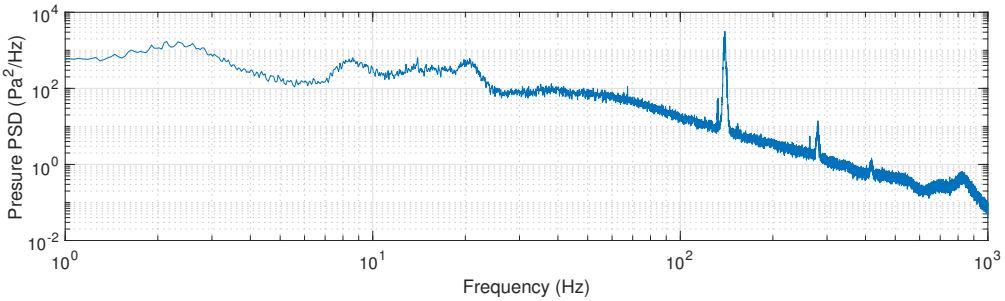

Figure 4.7: Pump pressure spectrum measured at the first pressure sensor with the rest of the circuit connected.

4.3. Model setup

A model has been devised to predict the plate vibrations when a driving pressure is applied at the input. The entire model will be solved by using finite elements in COMSOL Mulitpysics. The plate and dynamic links are now included, contrary to the model presented in chapter 3.3. The fluid-structure interaction on the plate is modelled by using bi-directional coupling and the dynamic links are modelled by solving the the 1-dimensional water hammer equations (eq 2.2 and 2.3). These equations are solved with finite elements instead of analytically, which makes it easier to couple the dynamic links to the rest of the model.

The plate is modelled by using 3-dimensional structural elements. The model has been simplified by removing the holes in the plate and by only modelling the lower part of the support brackets. The plate is meshed with relatively coarse tetrahedra elements and the mass of the accelerometers and signal amplifiers have been added manually. The model consists out of 146508 DOFs and a frequency sweep has been made to obtain the frequency response. The sweep has again been refined at the resonances. The entire model is linear, meaning that increasing the input pressure by a factor two will also increase the acceleration magnitude by the same amount. An elaborate explanation of the model setup is given in appendix G.

4.4. Measurement results

The experimental results will be compared to the model to verify the model's performance. Accelerations on the plate induced by the pump have been measured and the results are presented in this section.

Figure 4.8 presents the frequency response function (FRF) regarding the relation between the output pressure of the pump p_1 and the plate acceleration in the x- and z-direction (see figure 4.1 for a schematic overview). The plot shows both the measured and modelled results. The measured FRF's have been obtained with an H2-estimator for the same reason as given in section 2.6.

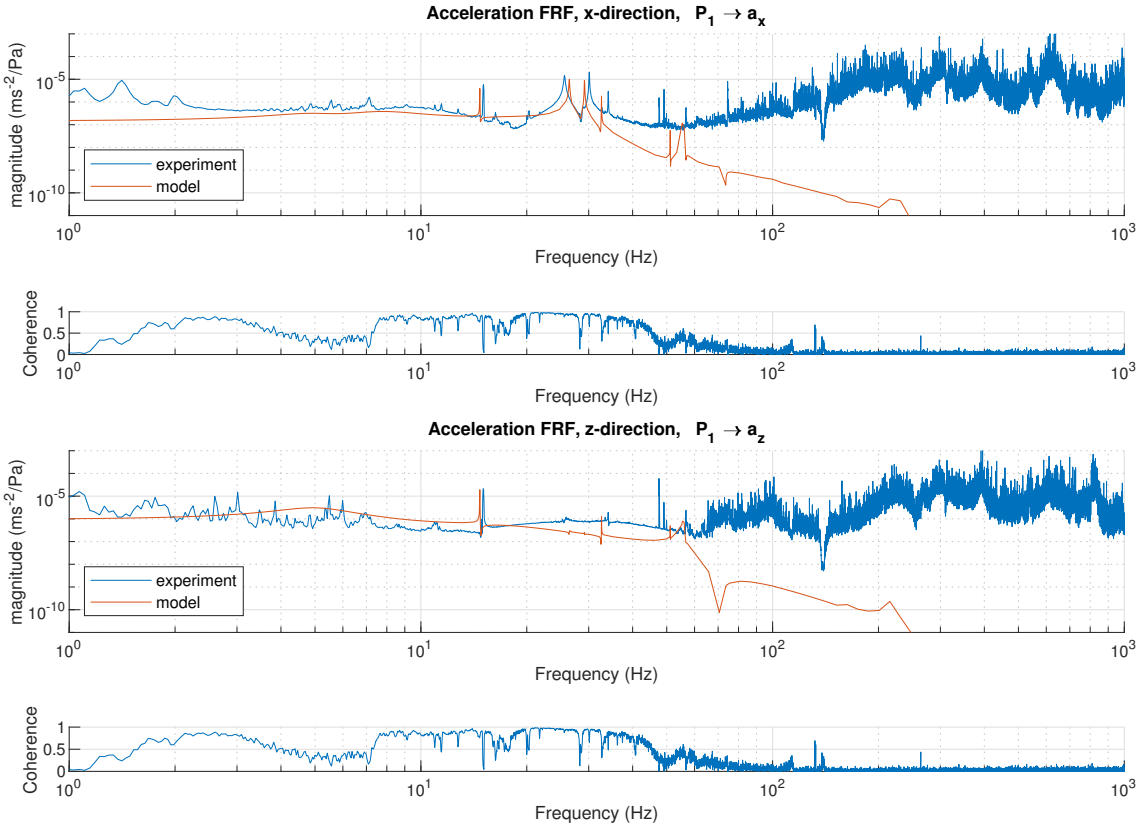

Figure 4.8: Frequency response between the input pressure and the plate acceleration.

The FRF for the x-direction shows resonance peaks at 26.4Hz and 29.3Hz while the response in the z-direction shows a peak at 14.9Hz. This behaviour is also predicted by the model. The resonances are the result of an eigenmode excitation by the fluid pressure. The first four eigenmodes of the plate and the tube

are shown in figure 4.9, simulating the tube and plate mechanics with added water mass. The first eigenmode predominantly excites the tube in the z-direction. The FRF peak is, therefore, most apparent in the z-direction. The opposite holds for the second and third eigenmode. These eigenmodes mainly show displacements in the xy-plane.

The model predicts a pressure reduction at high frequencies due to the viscoelastic behaviour of the dynamic links. However, the experimental results do not affirm this behaviour. The coherence of the measurement drops off after 50Hz. The measurement shown in figure 4.6 shows that the presence of flow increases the plate vibration up to 380Hz. It is possible that another unaccounted disturbance source is present on the plate. This disturbance may be generated by one of the couplings.

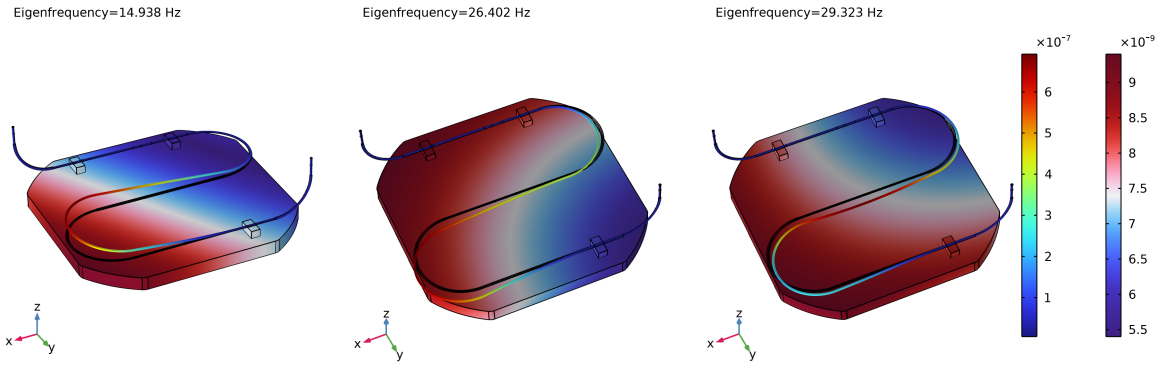

Figure 4.9: Deformation plot of the first 3 eigenfrequencies in meters. Separate colour scales are adopted for the plate and the tube. The 14.9 and 33.2 Hz eigenmodes show deformations in the z-direction while the 26.3 and 29.3 Hz modes show deformations in the xy-plane.

The transfer between the pump input and the plate acceleration consists of two subcomponents (see figure 4.10), namely the fluid behaviour in the dynamic link and the fluid structure interaction at the plate. The pressure behaviour in the dynamic links is given by the frequency response function between the pressure at the input p_1 and the plate p_2. This FRF is shown in figure 4.11.

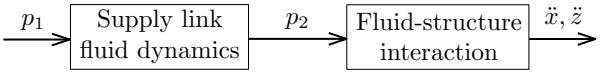

Figure 4.10: The transfer function between the pump and the plate can be subdivided into two parts.

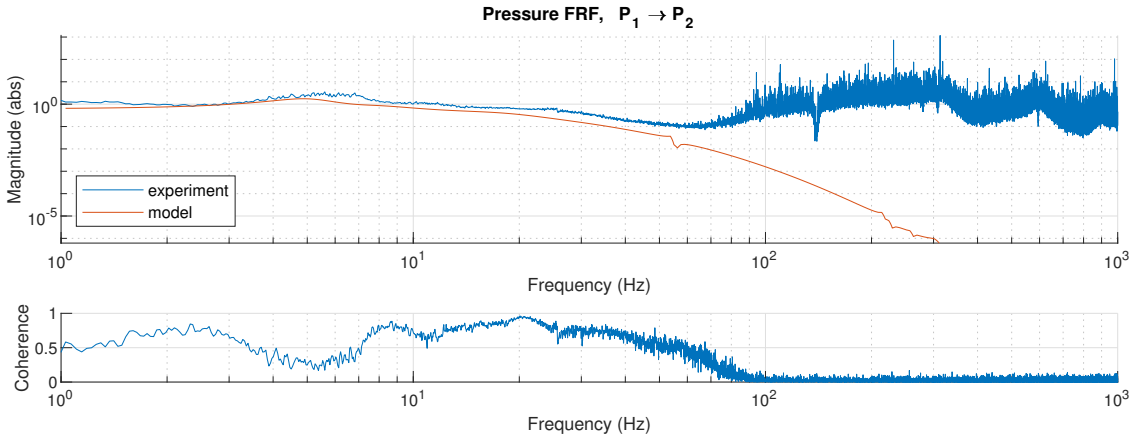

Figure 4.11: Transfer function between the pressure at the input p_1 and at the plate p_2.

The results show the same discrepancy between the model and the experimental results from around 50Hz: the coherence drops to zero and the magnitude defaults to noise. The same is also observed when looking at the power spectral density of the pressure. Figure 4.12 shows the the power spectral density of the measured input pressure p_1 and the pressure on the plate p_2. Furthermore, the figure shows the predicted

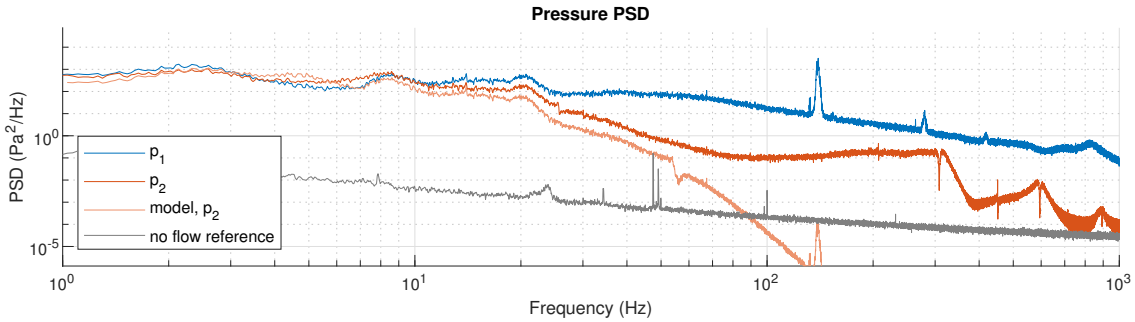

Figure 4.12: Power spectral density (PSD) of the pressure at the input p_1 and at the plate p_2. Both the measured and modelled pressures of p_2 are shown.

pressure on the plate based on the input pressure, according to equation 2.40. The results show that the measured and modelled pressure on the plate start to deviate significantly below a value of $1 \times 10^{-1}\,\mathrm{Pa}^2/\mathrm{Hz}$. A similar behaviour was also observed in section 2.6.

The fluid structure interaction on the plate is characterized by the FRF between the pressure on the plate p_2 and the plate acceleration $\ddot{x}, \ddot{z}$. This FRF is shown in figure 4.13. This model is able to give a good prediction of the FRF, also at frequencies above 50Hz.

Dynamic error budgeting (DEB) will used to derive the total disturbance magnitude caused by pump induced disturbances. DEB offers a convenient method to gain insight into the spectral behaviour of a disturbance. The power spectral density (PSD) and the cumulative power spectrum (CPS) for the plate acceleration in the x- and z-direction are shown in figure 4.14. The CPS is obtained by integrating the PSD signal. The PSD can be calculated with two methods: by using the pressure at the input p_1 or by using the pressure at the plate p_2, see equations 4.4 and 4.5.

$$PSD_{\ddot{x},\ddot{z}}(f) = \left|G_{p_1 \to \ddot{x},\ddot{z}}(f)\right|^2 \cdot PSD_{p_1}(f) \tag{4.4}$$

$$PSD_{\ddot{x},\ddot{z}}(f) = \left|G_{p_2 \to \ddot{x},\ddot{z}}(f)\right|^2 \cdot PSD_{p_2}(f) \tag{4.5}$$

The first method considers the entire setup including dynamic links, while the second method only models the fluid-structure interaction and dynamics of the plate. Both models are shown in the figure together with the measurement results. The PSD presented earlier in figure 4.6 showed the presence of suspension frequencies below 4Hz. The focus of this research lies on analysing disturbances generated by pressure pulsations. Therefore, the CPS plot has been integrated from 4Hz to eliminate the contribution of suspension frequencies below this frequency.

At low frequencies, both models are able to accurately predict the PSD magnitude. However, from 50Hz the model based on p_1 strongly deviates from the measurement. This can be attributed to deficiencies in the fluid model: the fluid model over-predicts the pressure decay in the dynamic links at high frequencies. Furthermore, it is observed that the vibration magnitude strongly builds up at the mechanical resonances of the plate. The model is able to predict the frequency of the resonances accurately, however the height of the peaks is hard to predict. The results show that the CPS increase at the resonances is calculated inaccurately. This is especially apparent when looking at the x-acceleration between 25 and 30 Hz.

To determine the standard deviation of the overall disturbance, the root of the total CPS should be taken [22]. The predicted and measured acceleration magnitudes are shown in table 4.1.

	x-direction	**z-direction**
Modelled based on p_1	$5.02 \times 10^{-5}\,\mathrm{m/s^2}$	$9.60 \times 10^{-5}\,\mathrm{m/s^2}$
Modelled based on p_2	$9.60 \times 10^{-5}\,\mathrm{m/s^2}$	$11.44 \times 10^{-5}\,\mathrm{m/s^2}$
Measured	$9.87 \times 10^{-5}\,\mathrm{m/s^2}$	$6.83 \times 10^{-5}\,\mathrm{m/s^2}$

Table 4.1: Measured and predicted acceleration magnitudes

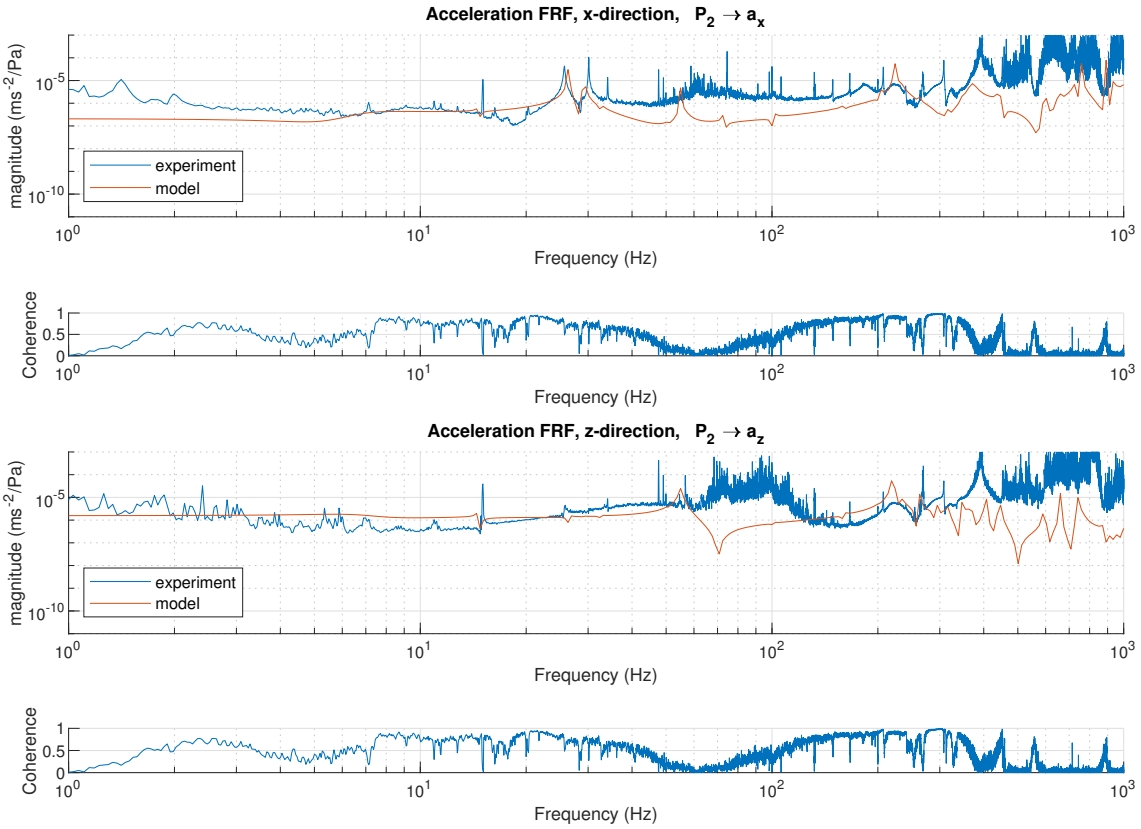

Figure 4.13: Transfer function between the pressure and acceleration on the plate

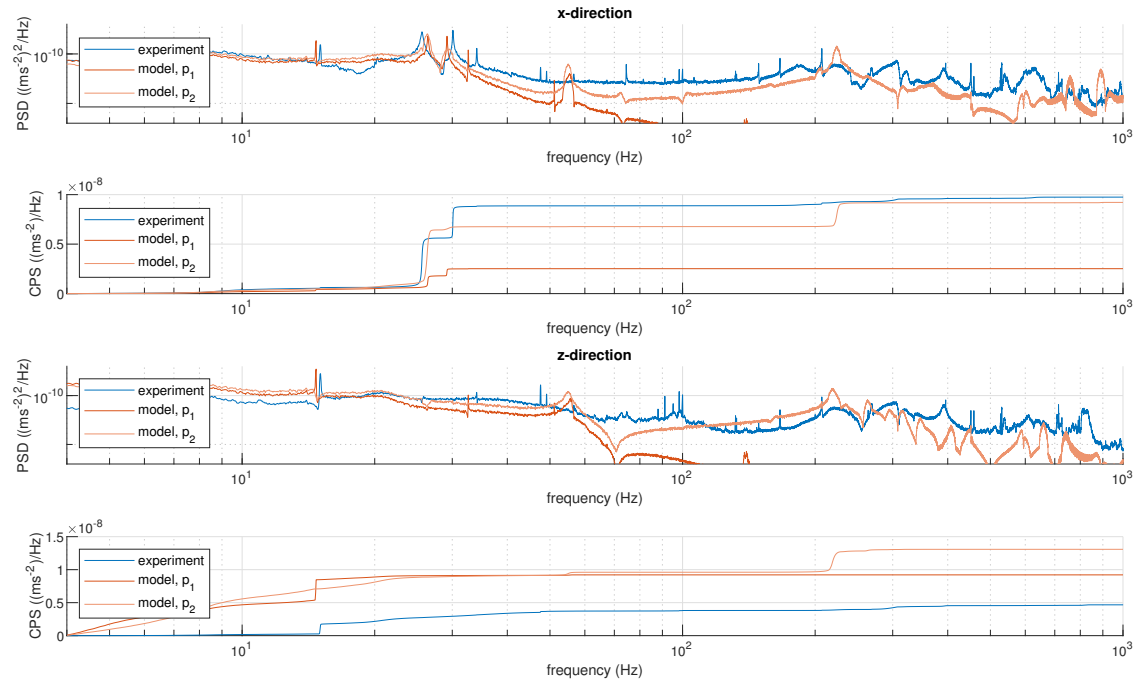

Figure 4.14: Power spectral density (PSD) and cumulative power (CPS) of the plate acceleration in the x- and z-direction. The experimental result is shown together with two model. One model is computed from the input pressure p_1 and the other model is computed from the pressure on the plate p_2.

4.5. Cooling circuit design optimization

Design improvements to the cooling system can be made based on the understanding gained in this research. The experimental setup will be modified to incorporate two possible improvements: adding more supports to the tube or increasing the length of the viscoelastic supply link. The measurement results will be compared to the modelled predictions for both situations.

In the previous section it was shown that significant jumps in the CPS magnitude occur at the mechanical eigenfrequencies of the plate. The eigenfrequencies of the steel conduit will be higher when additional supports are added. This may push the modes into a frequency region in which the dynamic links generate a sufficient amount of damping. The first mechanical eigenfrequency occurs at 51Hz when 6 supports are used to mount the tube. A schematic overview of the modified setup with 6 supports is shown in figure 4.15. A CAD drawing of the conduit with 6 supports is shown in figure 4.16. The model based on the output pressure of the pump predicts an acceleration reduction of 65% in the x-direction and 15% in the z-direction. The experimental results show an acceleration reduction of respectively 47% and 0%, which shows that the model over-predicts the acceleration decrease. A more detailed comparison between the model and experimental results is given in appendix H.

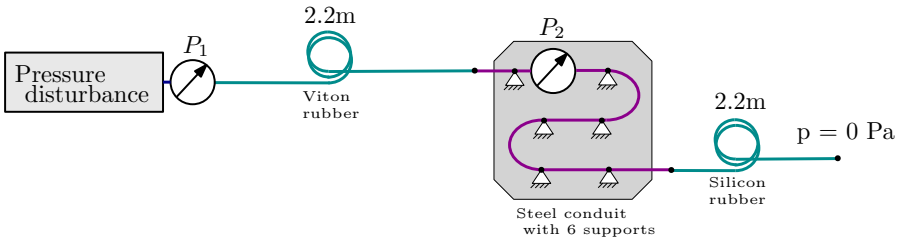

Figure 4.15: Setup with six supports

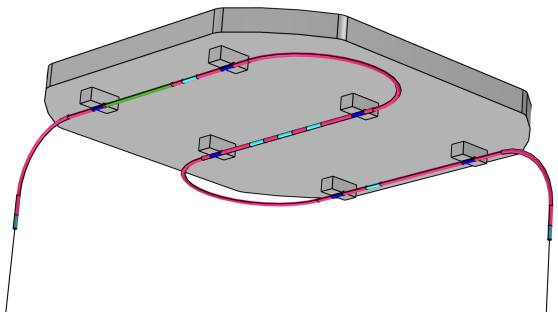

Figure 4.16: Fluid conduit with 6 supports. The light blue parts of the tube mark the locations of the fluid couplings and the green section marks the location of the pressure sensor manifold.

Another potential improvement can be made by adding more viscoelastic tubes before the steel conduit. In section 2.5, it was shown that adding viscoelastic tubes after the conduit is irrelevant for creating a more pressure decay, but adding viscoelastic tubing before the conduit was shown to be very effective. The supply link has been extended by adding viton rubber and silicon rubber tubing. A schematic overview of the altered setup is shown in figure H.2. The model based on the output pressure of the pump $p2$ predicts a magnitude reduction of 63% in the x-direction and 85% in the z-direction. The experimental results show a reduction of respectively 33% and 37%. A more detailed comparison between the model and experimental results is given in appendix H.

The measurements results of the three different configurations (see figure 4.1, 4.15 and 4.17) are compared with each other in figure 4.18. The figure shows the PSD and CPS values for the x- and z-direction, in which the CPS is taken from 4Hz.

The results show that the acceleration peaks at 14.9, 26.4 and 29.3Hz are not present for the conduit with six supports. The first mechanical resonance frequency at 51Hz is not observed in the acceleration data.The peaks at 14.9, 26.4 and 29.3Hz are still present when looking at the graph for the extended viscoelastic tube with 3 supports. However the peaks barely result into an increase of the CPS. Furthermore, it is also apparent

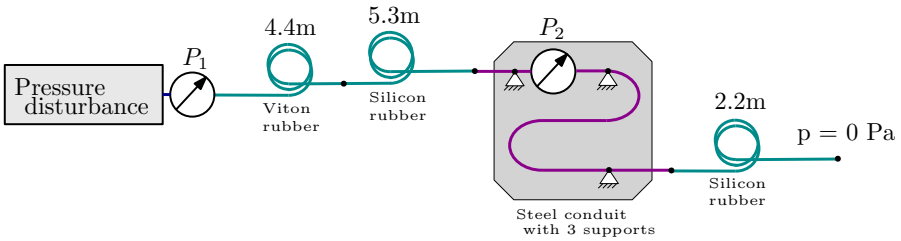

Figure 4.17: Setup with extended viscoelastic tubes

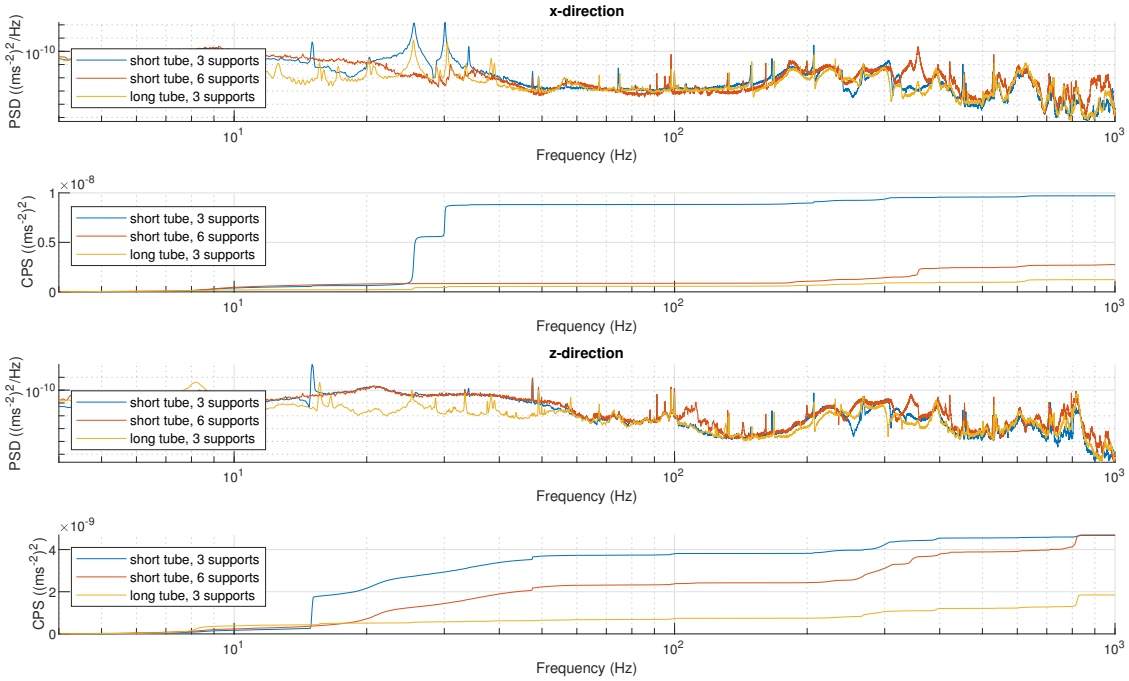

Figure 4.18: Power spectral density (PSD) and cumulative power (CPS) of the measured plate acceleration in the x- and z-direction. The results for 3 different configurations are shown.

that the level of broad band noise between 15 and 60 Hz is lower when looking at the z-direction. As a result, the build up in CPS is reduced.

5

Discussion

Based on the knowledge acquainted in this research, a set of design guidelines can be drafted to aid engineers in the mechanical design of cooling systems. The design of a cooling circuit may meet all the thermal requirements, however the designer should also ensure that vibrations generated by the cooling system are within the error budget. A schematic overview of a cooled precision system was shown in figure 1.1. This research considers a system with the following properties.

- The pressure disturbances are generated by a chiller at the inlet of the cooling circuit. Other components in the cooling circuit do not generate flow induced vibrations. The chiller is treated as a blackbox disturbance source, which will be characterized experimentally. Measurements show that the chiller generates a broadband pressure noise, which can be approximated by 1st order low pass filter.
- The pressure disturbances at the in- and output are decoupled and therefore uncorrelated. This means that pressure resonances at the circuit outlet cannot be propagated to the inlet.
- Flexible tubes are used between the chiller and the cooling conduit of the precision system. This approach is generally used for vibration isolated precision instrumentation. The flexible links serve two purposes: they mechanically isolate the system from it's surroundings and they impose damping on the pressure pulsations.
- The pressure at the circuit output is imposed to be zero, in order to establish a well defined boundary condition.
- The cooling conduit on the precision system consists of circular metal tubes, which are fixed to the system by a certain number of supports.

Considerations about the thermal design of the system are not a topic of this study. This research only concerns the transmission of pump induced vibrations to precision instrumentation.

The use of dynamic links is an important tool for designers to reduce the transmission of pump induced vibrations. These links provide damping to the pressure resonance peaks. Furthermore, the presence of the viscoelastic supply link provides a pressure decrease at high frequencies. The pressure is shown to decay exponentially over frequency according to formula 2.37. Only the supply links aid in providing a pressure attenuation, the return links are irrelevant for this effect. Materials with a high loss-modulus and a low storage modulus are most effective in adding a pressure decay (see figure 2.7). Viton rubber tubes are well suited as viscoelastic links, due to their excellent damping characteristics.

The disturbance magnitude strongly builds up around the mechanical eigenmodes of the conduit. Therefore, the cooling system should be designed such that viscoelastic links provide enough damping at these modes. This can be achieved by tuning the eigenfrequencies or by adjusting the length, diameter and wall thickness of the viscoelastic supply link. The first eigenfrequency of the conduit can be increased by adding more supports. This may push the first mode into a frequency region in which the viscoelastic link provides enough pressure attenuation. Alternatively, a different supply link can be used. Figure 5.1 shows the effect of the tube length, diameter and thickness on the pressure decay for a viton rubber supply tube. The results are obtained by using equation 2.37. The contour lines show the frequencies at which the pressure is attenuated

by a factor 10 or 100. The tube inner diameter divided by the wall thickness (D/e) is plotted on the y-axis and the tube length (x) is plotted on the x-axis.

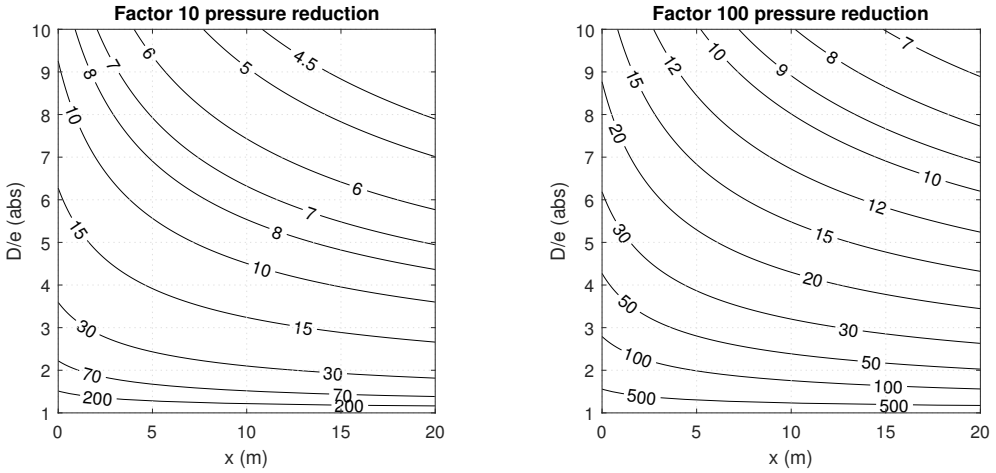

Figure 5.1: The pressure decay of a viton rubber supply link with tube inner diameter D, tube thickness e and tube length x. The contour lines show the frequency in Hz at which the pressure is attenuated by a factor 10 or 100. The inner diameter divided by the wall thickness is given on the y-axis and the link length is given in the x-axis.

The plots show increasing the tube length and the ratio D/e help in providing more pressure attenuation at low frequencies. This figure can be used by designers to determine the dimensions of a viton rubber supply link to achieve a a certain pressure attenuation.

6

Conclusion and recommendations

6.1. Conclusion

Flow induced disturbances generated in a cooling circuit can be the dominant disturbance source in a precision system, influencing its performance. For designers it is vital to predict the disturbance magnitude on the system. Therefore this research was focussed on the following objective:

Predicting the transmission of pump induced vibrations to nano-precision instrumentation by using dynamic error budgeting

The transmission of pump induced vibrations can be subdivided into two parts: the propagation of pressure pulsations through the dynamic links and the fluid structure interaction between the fluid and the cooling conduit on the instrumentation. A model is constructed to model the pump transmission by using linear systems theory. The pressure characteristics of the pump are assumed to be known.

The fluid dynamics in the dynamics links are governed by the fundamental equations of one-dimensional water hammer. This system of partial differential equations consists of a continuity equation and a momentum equation. Solving the one-dimensional water hammer equations shows that pressure resonances and anti-resonances will occur in the tube. The frequency of these resonances is dependent on the tube length, diameter, thickness and material. When considering a viscoelastic tube, the theory shows that the pressure decays exponentially over frequency (see equation 2.37). The water hammer model has been verified with an experiment. Measurements have been performed on different viscoelastic polymers tube. The results show that the model is able to provide an excellent prediction of the pressure behaviour up to a certain frequency. The prediction is shown to deviate once the power spectral density of the fluid pressure drops below a value of $1 \times 10^{-2}\,\mathrm{Pa}^2/\mathrm{Hz}$.

The main interaction mechanism between the pressure pulsations in the fluid and the tube mechanics occurs due to the presence of bends in the cooling conduit. In a bend, the pressure acting on the tube wall generates a resultant fluid load (see equation 3.1). This fluid load excites the mechanics of the tube, resulting in resonances at the mechanical eigenfrequencies. Increasing the amount of bends and increasing the cross-sectional area of the tube will increase the resultant force magnitude. A bi-directional coupling model was used to model the interaction between the fluid dynamics and tube mechanics. This model has been validated with an experiment. Both the model and experimental results show that mechanical resonances in the tube influence the pressure distribution in the liquid around the mechanical eigenfrequencies of the tube.

The two modelling techniques above have been used to predict the disturbance magnitude of the setup introduced in the introduction (see figure 1.2). The setup is designed to be a representation of a simple precision system for which pump induced vibrations are the predominant disturbance force. Experiments have been performed on three different configurations and dynamic error budgeting has been used to compare the modelled and experimental results. When looking at the PSD of the plate acceleration, it is observed that the magnitude and resonance behaviour is well predicted up to a frequency of ~50Hz. Above this frequency, the acceleration is predicted to attenuate more than measured. This can be due to unaccounted flow induced disturbance sources in the circuit or it can be down to shortcomings in the dynamic link model. The total disturbance can be analysed by using the cumulative power spectrum (CPS). It is observed that the disturbance

magnitude strongly increases around the eigenfrequencies of the cooling conduit. The model is capable of giving a decent qualitative description of the spectral disturbance behaviour below ~50Hz. However, when looking at the total disturbance, the model is only capable give an order of magnitude estimation, because the magnitude of the resonances cannot be accurately predicted. The modelled, total disturbance is shown to deviate up to a factor 5 from the measured results. The longer the dynamic link, the worse the model will perform.

6.2. Recommendations

Several recommendations can be made to improve the predictability of the model. The predictability can be improved by making changes to the setup or by improving the model itself

The fluid behaviour in the dynamic links has currently been modelled by using the fundamental equations of 1D water hammer. In these equations, only the axial motion of the fluid is considered. The inertia and axial motion of the tube are neglected. The model can be enhanced by taking the radial expansion and the axial movement of the tube into account. A one-dimensional description of a liquid-filled tube including these degrees of freedom can be found in [6, 28]. Axial waves over the tube wall can be modelled when using this description. Alternatively, a 3-dimensional model with bi-directional coupling can be used to model the dynamic links. This method requires the designer to know the exact geometry of the links. The suspension modes of the links may also influence the plate acceleration at low frequencies.

The predictability can also be improved by altering the experimental setup, discussed in section 4.1. The plate is now suspended in an acoustic enclosure. Several improvements on the enclosure have been made. However, measurements show that the acoustic disturbances are still dominant at certain frequency ranges. Furthermore, the dynamic links may also be excited by room acoustics, which can potentially have a measurable effect on the plate acceleration. The setup can be improved by building an additional acoustic enclosure around the current enclosure. The new enclosure should have enough space to place the dynamic links inside.

Another improvement can be made by changing the design of the plate. The current plate is mostly excited by acoustic in the z-direction, because most of the surface area of the plate is located in the xy-plane. Future research can look into a different plate design, which is less sensitive to acoustic excitation.

Furthermore, there are several options to improve on the computation time of the model. Exploring these options may not be worth the effort when the model only needs to be run a few times. However, it will be relevant when one wants to run a lot of iterations or when the model is used to run an optimisation algorithm.

The frequency response function is currently computed by solving the model for a large number of frequencies. This requires a lot of computation time. An alternative would be to use the modal summation method. This method involves the calculation of the mode shapes (Ψ_n) and determining the contribution of each mode to the overall response. This contribution is referred to as the modal participation factor (P_n). The total response of the system can be computed by multiplying the mode shape with the participation factor and summing over all the modes, $\sum P_n \Psi_n$. The complicated behaviour can be represented by a weighted sum of a sufficiently large number of modes.

Another advance in computational efficiency can be made by reducing the model complexity. The model can be simplified from a 3-dimensional to a 1-dimensional description, significantly reducing the number of mesh elements. In this case the tube can be represented as a fluid filled beam by using the Euler-Bernoulli beam theory and the fluid-dynamics are governed by the fundamental equations of 1D water hammer. The designer should, however, always be aware of the model limitations when doing these simplifications.

Further research can be done on cooling systems with multiple flow induced disturbance sources. This would allow designers to model a cooling system containing a pump and several other irregularities generating pressure disturbances. Examples of irregularities include sharp corners, stepped diameter changes or sharp edges inside a fluid coupling. The disturbance magnitude generated by these kind of irregularities is currently unknown. Predicting this magnitude is a potential topic of further research.

A

Electrical analogy

An electrical analogy can be used to solve the water hammer equations given in equations 2.2 and 2.3. Equation 2.13 will be derived in this appendix. This equation describes the relation of pressure and flow between the input and a cross-section at coordinate x.

The circuit shown in figure A.1 represents a transmission line element of infinitesimal length ∂x.

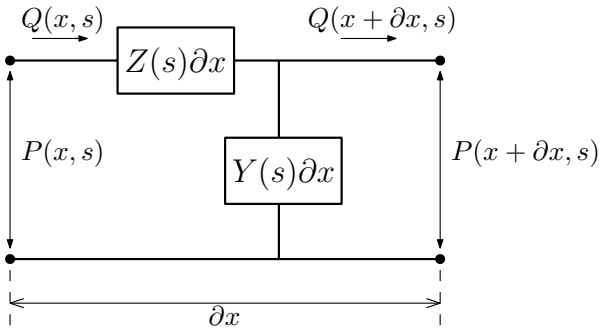

Figure A.1: Infinitesimal transmission line element

Using Kirchoff's node and loop laws, one can write

$$P(x,s) - Q(x,s)Z(s)\delta x - P(x+\delta x,s) = 0 \tag{A.1}$$
$$Q(x,s) - P(x+\delta x,s)Y(s)\delta x - Q(x+\delta x,s) = 0 \tag{A.2}$$

$$\frac{P(x,s) - P(x+\delta x,s)}{\delta x} = -Q(x,s)Z(s) \tag{A.3}$$
$$\frac{Q(x,s) - Q(x+\delta x,s)}{\delta x} = -P(x+\delta x,s)Y(s) \tag{A.4}$$

$$P_x(x,s) = -Z(s)Q(x,s) \tag{A.5}$$
$$Q_x(x,s) = -Y(s)P(x,s) \tag{A.6}$$

Deriving with respect to x

$$P_{xx}(x,s) = -Z(s)Q_x(x,s) \tag{A.7}$$

Plugging in $Q_x(x,s)$

$$P_{xx}(x,s) = Y(s)Z(s)P(x,s) \tag{A.8}$$

When plugging in the values of $Y(s)$ and $Z(s)$ (see equation 2.17) the equation becomes $P_{xx}(x,s) = s^2/a^2 P(x,s)$. This form is well known as the wave equation with a being the wave speed. Solving eq A.8 gives

$$P(x,s) = A_1 e^{\sqrt{Z(s)Y(s)}x} + A_2 e^{-\sqrt{Z(s)Y(s)}x} \tag{A.9}$$

$$Q(x,s) = -A_1\sqrt{Y(s)/Z(s)}Z e^{\sqrt{Z(s)Y(s)}x} + A_2\sqrt{Y(s)/Z(s)}e^{-\sqrt{Z(s)Y(s)}x} \tag{A.10}$$

The propagation constant Γ and the characteristic impedance Z_c will be defined for easier notation.

$$\Gamma(s) \equiv \sqrt{Z(s)Y(s)} \tag{A.11}$$

$$Z_c \equiv \sqrt{Z(s)/Y(s)} \tag{A.12}$$

When using boundary conditions $P|_{x=0} = P_i$ and $Q|_{x=0} = Q_i$, A_1 and A_2 will become

$$A_1 = \frac{1}{2}(P_i - Z_c Q_i) \tag{A.13}$$

$$A_1 = \frac{1}{2}(P_i + Z_c Q_i) \tag{A.14}$$

Plugging this into equations A.9 and A.10 gives

$$P(x,s) = \frac{1}{2}(P_i - Z_c Q_i)e^{\Gamma x} + \frac{1}{2}(P_i + Z_c Q_i)e^{-\Gamma x} \tag{A.15}$$

$$Q(x,s) = \frac{1}{2}(Q_i - Z_c^{-1} P_i)e^{\Gamma x} + \frac{1}{2}(Q_i + Z_c^{-1} P_i)e^{-\Gamma x} \tag{A.16}$$

Rearranging gives

$$P(x,s) = P_i\frac{e^{-\Gamma x} + e^{\Gamma x}}{2} - Z_c Q_i\frac{e^{-\Gamma x} + e^{\Gamma x}}{2} \tag{A.17}$$

$$Q(x,s) = Z_c^{-1} P_i\frac{e^{-\Gamma x} + e^{\Gamma x}}{2} + Q_i\frac{e^{-\Gamma x} + e^{\Gamma x}}{2} \tag{A.18}$$

$$P(x,s) = P_i\cosh(\Gamma x) - Z_c Q_i\sinh(\Gamma x) \tag{A.19}$$

$$Q(x,s) = Z_c^{-1} P_i\cosh(\Gamma x) + Q_i\sinh(\Gamma x) \tag{A.20}$$

This can be rewritten into the following convenient matrix form

$$\begin{bmatrix} P(x,s) \\ Q(x,s) \end{bmatrix} = \begin{bmatrix} \cosh\big(\Gamma(s)x\big) & -Z_{\mathrm{c}}(s)\sinh\big(\Gamma(s)x\big) \\ -Z_{\mathrm{c}}(s)^{-1}\sinh\big(\Gamma(s)x\big) & \cosh\big(\Gamma(s)x\big) \end{bmatrix} \begin{bmatrix} P_{\mathrm{i}}(s) \\ Q_{\mathrm{i}}(s) \end{bmatrix} \tag{A.21}$$

B

Transmissionline modeling

An analytical expression for the fluid transient behaviour of a fluid in a tube can be derived by using transmission line modelling. In this appendix, the transfer function between the pressure at a chosen location on the tube p_x and the input pressure p_i is derived. A schematic of a transmission line is shown in figure B.1. As mentioned before, the transfer function can be derived by using the following relation $P_x/P_i = (P_x/P_L)(P_L/P_i)$.

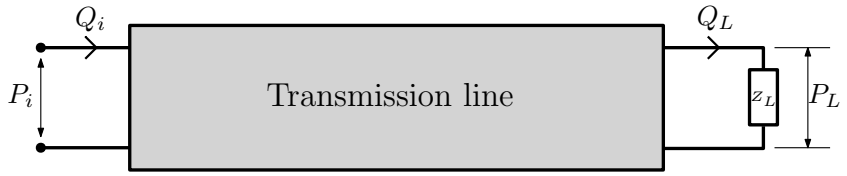

Figure B.1: Schematic representation of a transmission line with load impedance Z_L. The block represents an infinite number of line elements as shown in figure A.1.

Using matrix equation A.21 derived in appendix A and taking the inverse gives

$$\begin{bmatrix} P_{\mathrm{i}}(s) \\ Q_{\mathrm{i}}(s) \end{bmatrix} = \begin{bmatrix} \cosh\Gamma(s)x & -Z_{\mathrm{c}}(s)\sinh\Gamma(s)x \\ -Z_{\mathrm{c}}(s)^{-1}\sinh\Gamma(s)x & \cosh\Gamma(s)x \end{bmatrix}^{-1} \begin{bmatrix} P(x,s) \\ Q(x,s) \end{bmatrix} \tag{B.1}$$

$$\begin{bmatrix} P_{\mathrm{i}}(s) \\ Q_{\mathrm{i}}(s) \end{bmatrix} = \begin{bmatrix} \cosh\Gamma(s)x & Z_{\mathrm{c}}(s)\sinh\Gamma(s)x \\ Z_{\mathrm{c}}(s)^{-1}\sinh\Gamma(s)x & \cosh\Gamma(s)x \end{bmatrix} \begin{bmatrix} P(x,s) \\ Q(x,s) \end{bmatrix} \tag{B.2}$$

Writing down the first row of equation B.2 at $x = l$ using $Q_o = P_o/Z_L$ yields

$$P_i = P_o\cosh(\Gamma l) + P_o\frac{Z_c}{Z_L}\sinh(\Gamma l) \tag{B.3}$$

This can be rewritten to obtain the transfer function from the pipe input to output

$$\frac{P_o}{P_i} = \frac{1}{\cosh(\Gamma l) + \frac{Z_c}{Z_L}\sinh(\Gamma l))} \tag{B.4}$$

Deriving the transfer function from spatial coordinate x to the output of the pipe gives

$$\frac{P_x}{P_o} = \cosh(\Gamma(l-x)) + \frac{Z_c}{Z_L}\sinh(\Gamma(l-x))) \tag{B.5}$$

Multiplying equations B.4 and B.5 gives the final transfer function

$$\frac{P_x(s)}{P_i(s)} = \frac{\sinh\Gamma(s)(l-x) + \frac{z_l}{z_c}\cosh\Gamma(s)(l-x)}{\sinh\Gamma(s)l + \frac{z_l}{z_c}\cosh\Gamma(s)l} \tag{B.6}$$

C

Fluid viscosity

The effect of fluid viscosity is assumed to be negligible compared to the damping imposed by a viscoelastic tube and therefore, this effect has not been taken into account in this research. This appendix explains why fluid viscosity can be neglected by means a few examples.

The effect of fluid viscosity can be incorporated into the transmission model by adapting the propagation factor Γ and the characteristic impedance Z_c. This has been done by assuming average friction and using the absolute fluid viscosity μ. A derivation for the adapted values of Γ and Z_c can be found in [14].

Lossless line	**Average friction**
$\Gamma(s) = \frac{s}{a}$	$\Gamma(s) = \frac{1}{a}\sqrt{\frac{8\pi\mu}{\rho A}\frac{1}{s}+1}$
$Z_c(s) = \frac{\rho a}{A}$	$Z_c(s) = \frac{\rho a}{A}\sqrt{\frac{8\pi\mu}{\rho A}\frac{1}{s}+1}$

The term $\frac{8\pi\mu}{\rho A}$ shows that fluid damping is more prevalent at low frequencies when the absolute viscosity μ is high and the density ρ and cross-sectional area A are low. The transfer functions of water and oil in a steel tube is shown in figure C.1. The tube has the same properties as detailed in table 2.1, except that it is assumed here that the steel has a damping tangent of 0.005. Both the transfer functions with and without fluid viscosity have been plotted.

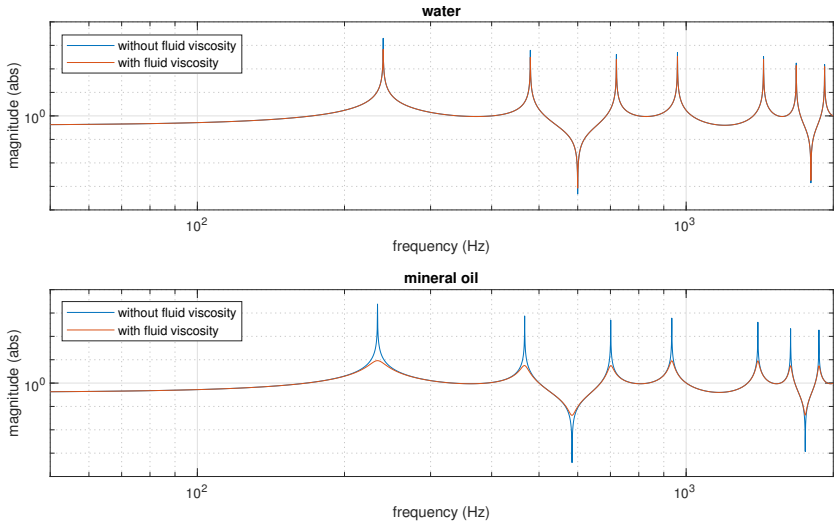

Figure C.1: FRF between p_i and p_x for water and mineral oil, modelled with and without viscosity. The fluid is conveyed through a steel tube.

The results show that the additional damping introduced by fluid viscosity in water is fairly low. The Q-factors of the first resonance peak with and without fluid viscosity are respectively 1.6×10^4 and 4.6×10^4. This difference will be even lower at higher frequency resonances. The effect of fluid viscosity is significant when looking at the fluid transient behaviour of mineral oil.

Several authors [2] have stated that the damping due to fluid viscosity is negligible compared to damping induced by the viscoelasticity of the tube. The fluid behaviour of a silicon rubber tube conveying water has been investigated to verify this claim. The pressure transfer function is shown in figure C.2. The behaviour with and without fluid viscosity has been plotted.

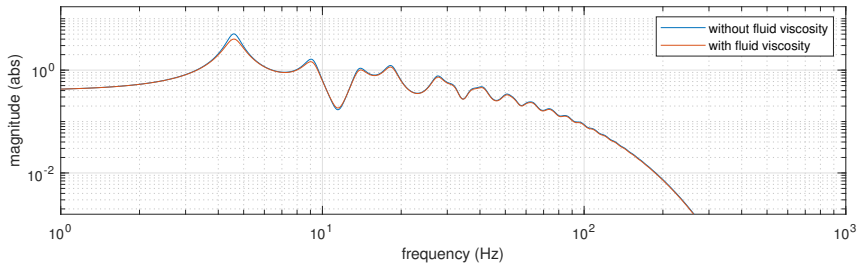

Figure C.2: FRF between p_i and p_x for water, modelled with and without viscosity. The fluid is conveyed through a PTFE tube.

It is observed that the difference between both models is fairly small. The Q-factors of the first resonance peak with and without fluid viscosity are respectively 9.4 and 11.8. The difference will be lower at higher frequencies. The Q-factors at the second resonance are calculated to be 3.3 with viscosity and 3.7 without viscosity.

From the examples above it can be concluded that fluid viscosity can be neglected for the tubes considered in this research. This assumption could not have been made if long tubes with a 1 mm diameter were considered.

D

Pressure sensor manifold

The PCB 112A22 has been selected to measure the fluid pressure inside the tube, see figure D.1. This sensor has a cylindrical shape with a electrical connector on one side and a sensing membrane on the other side. A fluid manifold has been designed to integrate the sensor in the circuit. The manifold is made such that the sensor does not protrude into the fluid to ensure that there are no sharp edges creating FIV. Therefore, the manifold has been designed with an organic shape, see figure D.2. The duct inside the manifold transitions from a circular cross section to cross-section with a flattened top, such that the pressure sensor can be mounted flush with this flat section.

Figure D.1: PCB 112A22. The sensing membrane is located at the bottom and the electrical connector at the top.

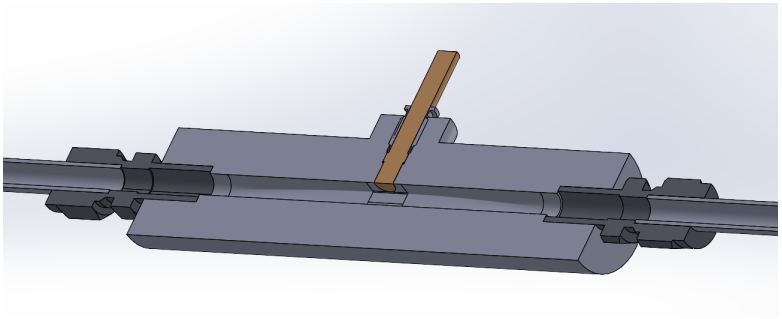

Figure D.2: CAD drawing of the sensor manifold. The sensor is shown with a different colour.

The manifold has been 3D-printed by using stereolithography (SLA), this technique is also known as resin printing. Parts are printed by solidifying a liquid with a laser in a layer by layer fashion. SLA printing is well suited for producing complex geometries with small features and tight tolerances. However, using SLA printing also has some downsides. For example, printing overhanging material presents a challenge, particularly when encountering holes with an axis aligned parallel to the printing layers. These holes will not be perfectly circular when printing them. A solution to address this issue is to print the part at an inclined angle. This will improve the circularity of the sensor hole. Furthermore, SLA-printed parts are known to shrink after printing. The sensor holes in the manifold were post machined to correct for the inaccuracies caused by the overhang and shrinkage. However, after post machining it still proved difficult to provide a leak tight seal with the sensor. The 3D-printed resin is very soft, which makes it easy to damage the countersink hole in the part when tightening the sensor. A leak tide seal was eventually achieved with some teflon tape.

In order to integrate the manifold into the fluid circuit, a clamp coupling from Swagelok has been glued into both sides of the manifold. The couplings are post machined in order to remove the stepped diameter changes inside it. This has been done to guarantee that there are no sharp edges. Two pressure sensors are used for the final setup: one is mounted after the pump while the other is mounted on the plate, see figure D.3. The designs of the manifold on the plate is slightly different to ensure that it fits in the tighter space. A picture of the duct inside the manifold is shown in figure D.4. It shows that the sensor slightly protrudes from

the duct wall. This could be a potential FIV source, but it is unknown if this source leads to a measurable contribution.

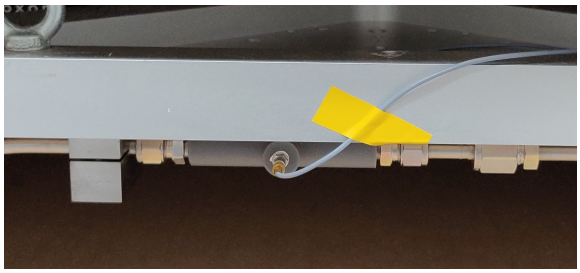

Figure D.3: Sensor manifold mounted below the plate.

Figure D.4: The the duct inside the manifold. It can be seen that the sensor slightly protrudes from the duct wall.

E

Resultant pressure load in curved tubes

The resultant pressure load per unit length of the tube centreline will be derived in this appendix. For this derivation, a curved tube with an infinitesimal angle $\Delta\phi$ will be considered, see figure E.1. The length of the tube centreline is called ΔL and the instantaneous centre of the tube is located at point O. Furthermore, the tube has a curvature radius R and inner diameter D_i. The x-axis is oriented normal to the tube centreline $\mathbf{n}$ and the y-axis is oriented perpendicular to the curvature angle $\Delta\phi$.

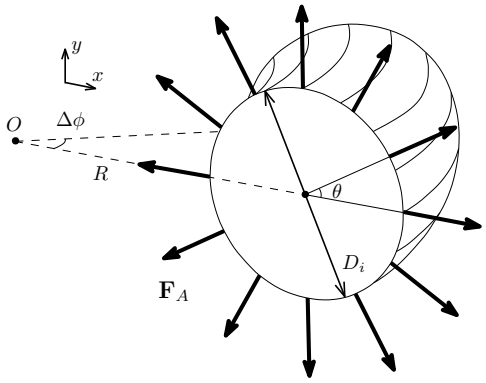

Figure E.1: Schematic overview of an infinitesimal curved tube section, with radius R, curve angle $\Delta\phi$ and diameter D_i. The arrows pointing outward depict the fluid pressure load at the tube wall $\mathbf{F}_A$.

The pressure load at the tube wall ($\mathbf{F}_A = p\mathbf{n}$) will generate a resultant force because the wall area at the outer side of the bend is greater than the area at the inner side. The expression for the resultant force can be derived by taking the integral of the pressure load $\mathbf{F}_A$ over the polar coordinate θ.

The resultant force in the x-direction can be evaluated as follows

$$\Delta F_x = \int_0^{2\pi} \left(\Delta L_\theta \cdot F_{x,\theta}\right) d\theta \tag{E.1}$$

with ΔL_θ being the arc length of the tube wall at coordinate θ and $F_{x,\theta}$ being the x-component of the fluid load $\mathbf{F}_A$ at the same coordinate. Plugging in the expressions for ΔL_θ and $F_{x,\theta}$ gives

$$\Delta F_x = \int_0^{2\pi} \left(\left(R + \tfrac{1}{2} D_i \cos\theta\right)\Delta\phi \cdot \tfrac{1}{2} D_i\, p \cos\theta\right) d\theta \tag{E.2}$$

Rewriting and integrating this expression gives

$$\Delta F_x = \int_0^{2\pi} \left(\tfrac{1}{2} R D_i \Delta\phi p \cos\theta + \tfrac{1}{4} D_i^2 \Delta\theta\, p \cos^2\theta\right) d\theta \tag{E.3}$$

$$= \left[\tfrac{1}{2} R D_i \Delta\phi p \sin\theta + \tfrac{1}{8} D_i^2 \Delta\theta\, p\left(\theta + \sin\theta\cos\theta\right)\right]_0^{2\pi} \tag{E.4}$$

$$= \tfrac{1}{4}\pi D_i \Delta\phi p \tag{E.5}$$

The same derivation can be made for the resultant force in the y-direction

$$\Delta F_y = \int_0^{2\pi} \left(\Delta L_\theta \cdot F_{y,\theta}\right) d\theta \tag{E.6}$$

$$= \int_0^{2\pi} \left(\left(R + \tfrac{1}{2} D_i \cos\theta\right)\Delta\phi \cdot \tfrac{1}{2} D_i\, p \sin\theta\right) d\theta \tag{E.7}$$

$$= \int_0^{2\pi} \left(\tfrac{1}{2} R D_i \Delta\phi\, p \sin\theta + \tfrac{1}{4} D_i^2 \Delta\theta\, p \sin\theta\cos\theta\right) d\theta \tag{E.8}$$

$$= \left[\tfrac{1}{2} R D_i \Delta\phi\, p \sin\theta + \tfrac{1}{8} D_i^2 \Delta\theta\, p\left(\theta + \sin^2\theta\right)\right]_0^{2\pi} \tag{E.9}$$

$$= 0 \tag{E.10}$$

The derivation shows that there is no resultant force in the y-direction, so the resultant force only acts in the x-direction. When using that $A = \frac{\pi}{4} D_i^2$ and $\kappa = \frac{1}{R}$ the fluid load per unit length f_L can be written as

$$\mathbf{f}_L = \frac{\Delta F_x}{\Delta L}\mathbf{n} \tag{E.11}$$

$$= A p \kappa \mathbf{n} \tag{E.12}$$

with A being the fluid's cross-sectional area, p the pressure amplitude, κ the curvature radius and $\mathbf{n}$ the normal of the tube centreline.

F

Acoustic disturbances

Measurements without fluid flow have been performed in order to assess the magnitude of the background vibrations. These vibrations are required to be as smaller than the pump induced disturbances. Earlier measurements have been performed with the setup in a different building. However, when moving into a new building, background disturbances have shown to be significantly stronger.

Several experiments have been performed to find the source of the background disturbances. From the results it was concluded that the disturbances are the results of acoustic noise. An acoustic enclosure has been designed to attenuate the acoustic disturbance and sound transmission loss (STL) theory has been used to design the enclosure. Eventually, three iterations have been made:

1. An enclosure with 18 mm thick MDF walls. A layer of insulation material has been applied at the inside of the enclosure. The insulation consists of 100 mm thick rockwool plates.
2. The same as iteration one, but a second 18 mm MDF wall has been installed inside the insulation.
3. The same as iteration two, but a layer of 10 mm plaster plates have been installed on the outside of the enclosure.

In this appendix, first, the background disturbances on the initial setup will be discussed, secondly, the basics of sound transmission theory will be covered and, lastly, the performance of the different enclosures will be evaluated.

F.1. Initial setup performance

A comparison between the acceleration measurements in the old and new building is shown in figure F.2. Both measurements were performed in the same cabinet to provide an equal comparison. A picture of the setup is shown in figure F.1. The measurements have been performed without any tubing connected to the plate.

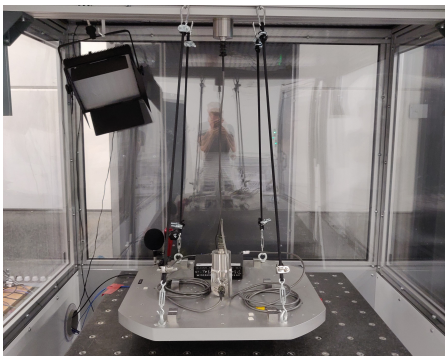

Figure F.1: Picture of the plate inside the cabinet.

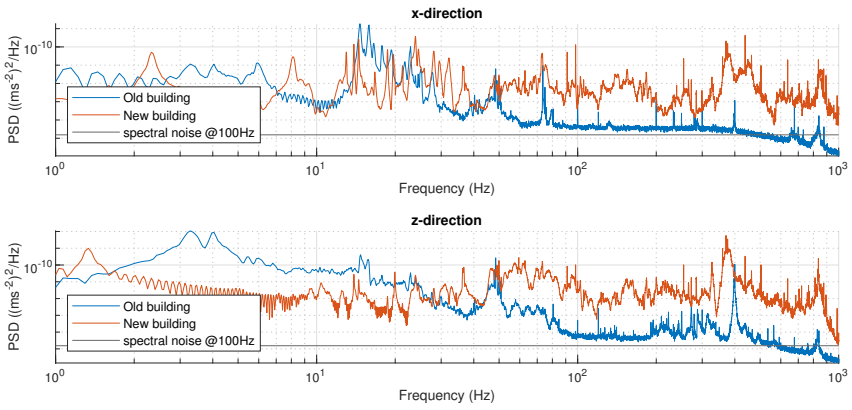

Figure F.2: Power spectral density plot of the plate acceleration in the x- and z-direction in the old and new building. The spectral noise of the sensor at 100Hz is also shown.

It is observed that the background noise is significantly worse with the new measurements, especially at higher frequencies.

F.2. Sound transmission loss

Sound transmission loss (STL) describes the decrease of sound intensity when a sound wave propagates through some type of structure [17]. STL is measured in dB as the relation between the total incident pressure on the structure P_i to the total transmitted pressure P_t

$$\Delta L_{TL} = -10\log\left(\frac{P_i^2}{P_t^2}\right) \tag{F.1}$$

The sound transmission loss through a panel is a function of the frequency of the sound wave. For a large frequency range, it is governed by the mass law. The mass law for a diffuse sound field reads

$$\Delta L_{TL} = 10\log(1+\frac{\omega m_s}{3.6\rho c}^2) \tag{F.2}$$

with m_s being the surface mass density, ρ the air density and c the speed of sound through air. The equation shows that panels with more mass per unit area provide more damping. The mass law of a double panel wall with an air cavity is given by

$$\Delta L_{TL} = 10\log\left(1+\left(\frac{\omega M}{3.6\rho c}-\frac{\omega^2 m_1 m_2}{(3.6\rho c)^2}\left(1-e^{-2ikd}\right)\right)^2\right) \tag{F.3}$$

with $m_{1,2}$ = the mass per unit area of an individual panel, M = the total mass per unit area, k = the wave number and d = the panel spacing. The theoretical sound transmission loss for the three enclosure iterations is plotted in figure F.3.

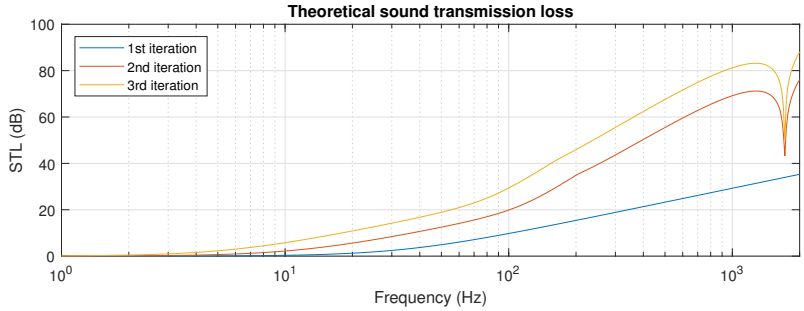

Figure F.3: Theoretical estimate of the STL for the three enclosure iterations.

The result shows that sound transmission loss at high frequencies can be achieved easily. However, improving the enclosure for low frequencies is a lot more difficult.

F.3. Acoustic enclosure

Pictures of the first and third iteration of the acoustic enclosure are shown in figure F.4. Measurements have been performed on the three iteration by measuring the sound pressure inside and by measuring the plate acceleration. The measurements results are given in figures F.5 and F.6.

(a) First iteration.

(b) Third iteration.

Figure F.4: Picture of two different enclosure iterations. The plate is not suspended in the enclosure in these figures.

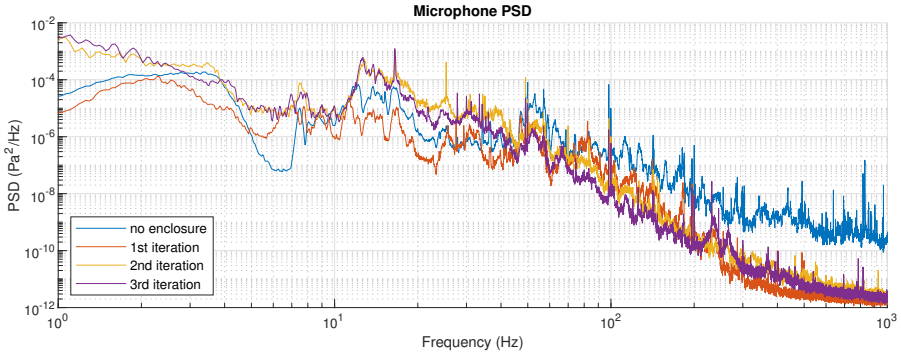

Figure F.5: Power spectral density plot of the sound pressure next to the plate.

Figure F.5 shows that the sound pressure magnitude does improve for every enclosure iteration. The sounds pressure attenuation also results in a reduction in background disturbances on the plate as shown in figure F.6. The acceleration level coincides with the sensor noise for some frequency ranges.

The 3rd iteration of the enclosure has been used in the final setup. However, it needed to be adjusted in order to incorporate the fluid circuit on the plate. The acoustic enclosure has been placed on legs and holes have been drilled in the bottom, see figure F.7. These adjustments did raise the background disturbance level. This is likely due to the relatively big holes in the bottom of the enclosure. These holes are need to suspend the dynamic links below the plate. The background disturbance level of the final setup can be found in chapter 4.2.

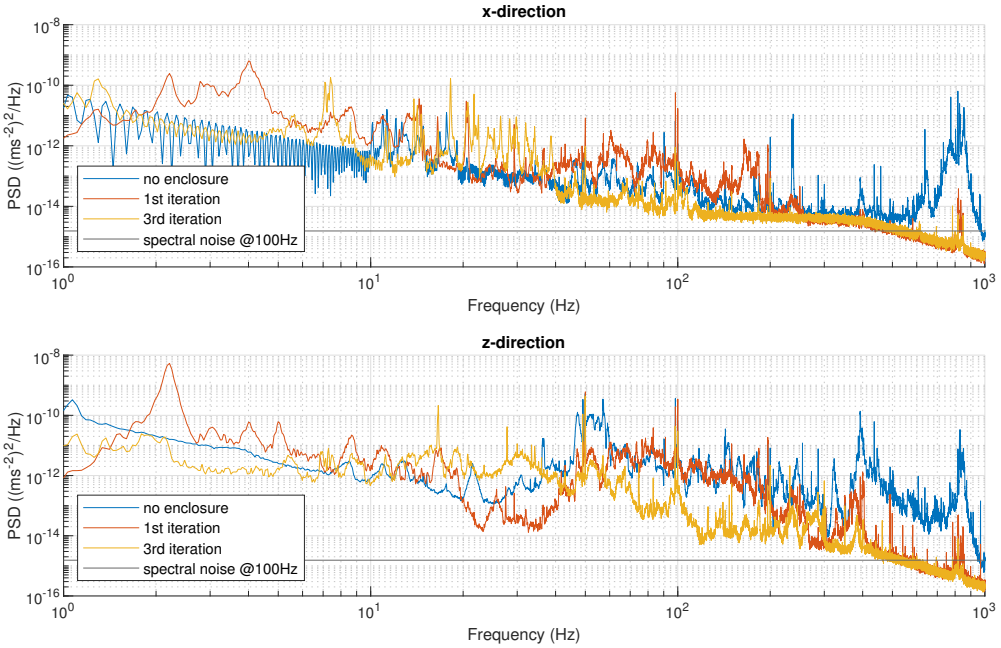

Figure F.6: Power spectral density plot of the plate acceleration in the x- and z-direction. The spectral noise of the sensor at 100Hz is also shown. The acceleration level coincides with the sensor noise for some frequency ranges.

Figure F.7: Enclosure with and without legs.

G

Comsol implementation

The finite element analysis has been performed with a software package called COMSOL Multiphysics. The software can be used to simulate various physics, but it especially excels at coupled phenomena and multi-physics. This appendix elaborates the setup of the finite element models used in the previous chapters.

G.1. Fluid transients in viscoelastic links

An analytic solution of the water hammer equations has been presented in chapter 2, but the equations can also be solved by using the finite element method in COMSOL. This can be done by using one of the build-in physics interfaces or by adding the equations manually.

The 'Pipe Acoustics, Frequency Domain' interface in COMSOL is able to compute the acoustic pressure and velocity variations when modelling the propagation of sound waves in flexible pipe systems. The model assumes that the propagating waves are plane. The governing equations are expressed in cross-sectional averaged variables, meaning that the tube is modelled over a 1-dimensional line, just as with the analytical model.

Alternatively, the pressure acoustics can be modelled by manually entering the one-dimensional water hammer equations into the the partial differential equation module of Comsol. To do this, equations 2.2 and 2.3 need to be transformed to the frequency domain

$$\frac{\partial V(i\omega)}{\partial x} = -\frac{i\omega}{\rho a^2} P(i\omega) \tag{G.1}$$

$$\frac{\partial P(i\omega)}{\partial x} = -\rho i\omega V(i\omega) \tag{G.2}$$

This system of differential equations can be solved by using the 'General form PDE' interface. The general form reads

$$e_a \frac{\partial^2 \mathbf{u}}{\partial t^2} + d_a \frac{\partial \mathbf{u}}{\partial t} + \nabla \cdot \left(-c\nabla \mathbf{u} - \alpha \mathbf{u} + \gamma \right) + \beta \cdot \nabla \mathbf{u} + a\mathbf{u} = f \tag{G.3}$$

with $\mathbf{u} = [V, P]^\top$ being the dependent variable that the program solves for. Casting equations G.1 and G.2 into G.3 gives

$$a = \begin{bmatrix} 0 & \frac{i\omega}{\rho a^2} \\ \rho i\omega & 0 \end{bmatrix}, \qquad \beta = \begin{bmatrix} 1 & 0 \\ 0 & 1 \end{bmatrix} \tag{G.4}$$

with the remaining coefficients $(e_a, d_a, c, \alpha, \gamma, f)$ being zero. This system of differential equations needs to be solved for a range of frequencies (ω) in order to obtain the frequency response. Another possibility would to use the Wave Equation interface with equation A.8. This will yield the same results.

G.2. Acoustic structure interaction

The interaction between the pressure acoustics in the fluid and the mechanics of the steel cooling conduit have been modelled in COMSOL. The geometry of the fluid column has been imported into the program. It consists of a curved solid cylinder with a diameter equal to the inner diameter of the tube. The 'pressure acoustics, frequency domain' interface is applied onto the cylinder's domain and the shell mechanics interface is added to the boundary of the cylinder. The thickness of the tube can be entered in one of the sub-menus. Here, the position should be chosen as 'Bottom surface on boundary' to make sure that the tube thickness is added on the outer side of the boundary.

A user-defined mesh has been applied on the tube. This made it possible to reduce the number of elements. First, a 'free triangular' mesh has been applied at the tube input face and in the next step this mesh is swept over the entire tube length. The tube centre-line has also been added in the geometry, to make it possible to generate plots along the arc-coordinate of this line. However, the presence of the centre line generates an error stating that 'the source has isolated entities'. Therefore a line should be added to connect the centre-line with the cylinder.

As mentioned in chapter 3, both a one-way and two-way model have been investigated. The one-way coupling is implemented in Comsol by applying the fluid pressure as a face load to the shell. In the face load submenu, select 'Bottom surface' under 'Through-Thickness location' to apply the load at the right location. The load type should be chosen as 'Force per unit area' and the load $\mathbf{F}_A$ should be set to 'acoustic load per unit area'. This option calculates the load magnitude as $\mathbf{F}_A = p\mathbf{n}$ in which $\mathbf{n}$ is the unit normal and p the pressure as calculated in the pressure acoustics interface. Selecting 'pressure' as the load type and directly entering the acoustic pressure will give wrong results. When implementing the one-way coupling, the fluid mass should be added manually. This can be achieved by adding mass to the shell boundary.

The two-way model has been implemented by using the build-in 'Acoustic-Structure Boundary' multiphysics interface. This coupling is easy to setup, only the boundary at which the coupling occurs should be selected. The fluid mass is automatically taken into account.

Both models have been solved for a frequency range from 1 till 1000Hz. The frequency samples are taken on a logarithmic scale with 100 samples per decade. However, the sampling has been improved around the resonances. All solver settings are automatically handled by Comsol. The program automatically selects a segregated stationary solver for the one-way model and a fully coupled stationary solver for the two-way model.

G.3. Plate model

The model simulating the final setup includes the steel conduit, the dynamic links and the plate. As mentioned in 4.3, fluid structure interaction is not taken into account for the dynamic links. Therefore, the links are modelled using the pipe acoustics interface, while the steel conduit is modelled by taking two-way coupling into account as described in the previous section. These parts are connected by using the 'Acoustic-Pipe Acoustic Connection' interface, which couples the pressure in the dynamic links to the pressure in the steel conduit.

Furthermore the plate is modelled by using the solid mechanics interface. A small rigid cube is added below the plate to represent the mass of the accelerometers. The mass of the amplifiers and cables on the plate is added over the volume of the entire plate. The plate and tube are coupled by using the 'Acoustic-Structure Boundary' interface. It is recommended to verify if the shell mechanics of the tube are connected to the plate. This can be done by plotting the expression `sshc1.i_conn` on the tube surface. The connectivity may fail when the tube mesh is too coarse.

G.4. Generating FRF plots

A bode plot of the FRF magnitude can easily be generated in COMSOL. For example, when plotting the pressure response from the input to another point on the circuit, this can be done by plotting the absolute value of the pressure amplitude (abs(p)) at the chosen location. Dividing by the input pressure is not strictly needed because the input pressure is set to unity.

Care should be taken when plotting quantities expressed as a resultant vector. This is due the method COMSOL uses to calculate the vector magnitude. For example, according to the equation view menu, the resultant acceleration in is computed as

$$\ddot{\mathbf{u}} = \sqrt{\mathrm{Re}(u_x)^2 + \mathrm{Re}(u_y)^2 + \mathrm{Re}(u_z)^2} \tag{G.5}$$

When using this expression, the behaviour of the frequency peaks is presented incorrectly. Therefore, the expression should be entered manually as

```
sqrt(solid.accX^2+solid.accY^2+solid.accZ^2)
```

H

Model validation for the optimized configurations

The experimental setup, introduced in chapter 4.3 has been modified to incorporate two potential improvements: adding more supports to the conduit and increasing the length of the viscoelastic supply link. A more detailed comparison between the model and experimental results is given in this appendix.

H.1. Adding more supports

The power spectral density (PSD) and the cumulative power spectrum (CPS) for the plate acceleration in the x- and z-direction are shown in figure 4.14. The PSD has been modelled in two different ways: by the using the pressure at the input p_1 and by using the pressure at the plate p_2. The model based on p_2 strongly overpredicts the overall disturbance, due to the resonance at 230Hz. This resonance coincides with the saddle mode of the plate. The measurement shows that this resonance is better damped than predicted by the model.

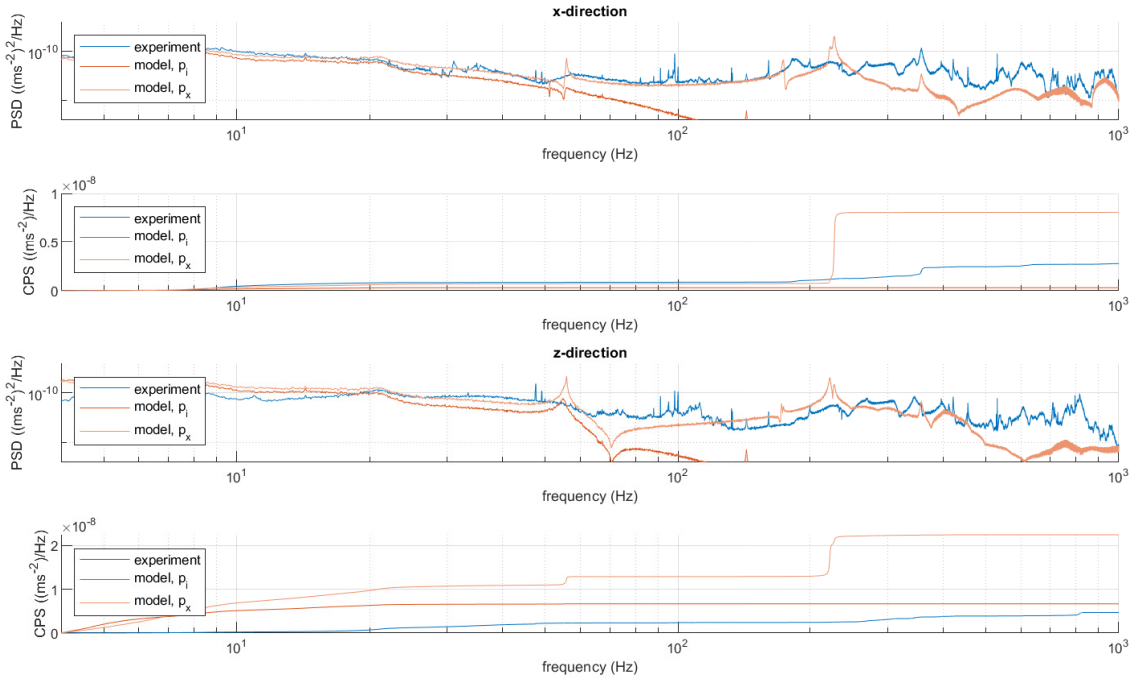

Figure H.1: PSD and CPS acceleration values for the configuration with 6 supports.

H.2. Increasing the length of the dynamic links

The PSD and CPS values for the x- and z-acceleration are again shown. The experimental results are presented together with the two different models. The results show that the model based on p_1 performs worse when considering longer viscoelastic supply links. The model based on p_2, again, strongly over-predicts the total acceleration magnitude due to the saddle mode of the plate.

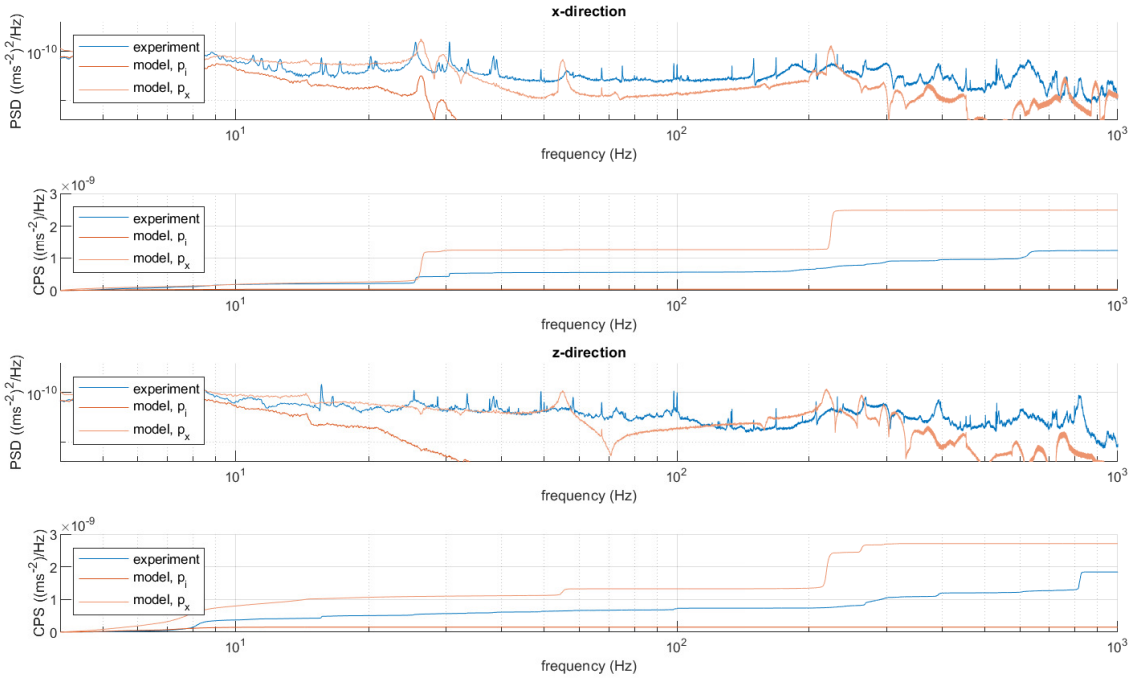

Figure H.2: PSD and CPS acceleration values for the configuration with longer dynamic links.

Bibliography

[1] Tijsseling AS. "Fluid-structure interaction in liquid-filled pipe systems: a review". In: *win.tue.nl* 10 (1996), pp. 109–146. URL: http://www.win.tue.nl/~atijssel/pdf_files/Tijsseling_1996.pdf.

[2] Dídia Covas et al. "The dynamic effect of pipe-wall viscoelasticity in hydraulic transients. Part I—experimental analysis and creep characterization". In: *http://dx.doi.org/10.1080/00221686.2004.9641221* 42 (5 2004), pp. 517–532. ISSN: 00221686. DOI: 10.1080/00221686.2004.9641221. URL: https://www.tandfonline.com/doi/abs/10.1080/00221686.2004.9641221.

[3] Korteweg DJ. "Ueber die Fortpflanzungsgeschwindigkeit des Schalles in elastischen Röhren". In: *scholar.archive.org* (1878). URL: https://scholar.archive.org/work/aklzj43yrbhd7afv2hcey5po3e/access/ia_file/crossref-pre-1909-scholarly-works/10.1002%252Fandp.18772360313.zip/10.1002%252Fandp.18782411206.pdf.

[4] Wylie EB and Streeter VL. *Fluid transients*. 1978. URL: https://ui.adsabs.harvard.edu/abs/1978mhi..book.....W/abstract.

[5] Allen Fagerlund et al. "Identification and prediction of piping system noise". In: *19th National Conference on Noise Control Engineering 2005, Noise-Con 05* 2 (2005), pp. 819–825. ISSN: 0001-4966. DOI: 10.1121/1.4779151. URL: https://www.researchgate.net/publication/242370106_Identification_and_prediction_of_piping_system_noise.

[6] D Ferras et al. "Fluid-Structure Interaction models in pressurized fluid-filled pipes: a review". In: (2018). URL: https://www.preprints.org/manuscript/201809.0049.

[7] Mohamed S Ghidaoui et al. "A review of water hammer theory and practice". In: *asmedigitalcollection.asme.org* (2005). DOI: 10.1115/1.1828050. URL: https://asmedigitalcollection.asme.org/appliedmechanicsreviews/article-abstract/58/1/49/458451.

[8] S.E. Isakoff. "Analysis of Unsteady Fluid Flow Using Direct Electrical Analogs". In: *Industrial & Engineering Chemistry* 47 (3 Mar. 1955), pp. 413–421. ISSN: 0019-7866. DOI: 10.1021/IE50543A027. URL: https://pubs.acs.org/doi/abs/10.1021/ie50543a027.

[9] Modisette J. *The Joukowsky Equation*. 2021. URL: https://www.atmosi.com/en/news-events/blogs/the-joukowsky-equation/.

[10] L. Jabben. *Mechatronic design of a magnetically suspended rotating platform*. 2007. URL: https://repository.tudelft.nl/islandora/object/uuid%3Ad2f37bb8-99c8-4cb9-9f97-ab28a807a178.

[11] Weinerowska-Bords K. "Viscoelastic model of waterhammer in single pipeline-problems and questions". In: *infona.pl* 53 (4 2006), pp. 331–351. ISSN: 1231-3726. URL: https://www.infona.pl/resource/bwmeta1.element.baztech-article-BAT8-0004-0026.

[12] Shigehiko Kaneko et al. "Flow-Induced Vibrations: Classifications and Lessons from Practical Experiences: Second Edition". In: *Flow-Induced Vibrations: Classifications and Lessons from Practical Experiences: Second Edition* (2013), pp. 1–410. DOI: 10.1016/C2011-0-07518-X. URL: http://www.sciencedirect.com:5070/book/9780080983479/flow-induced-vibrations.

[13] A. Keramat et al. "Fluid–structure interaction with pipe-wall viscoelasticity during water hammer". In: *Journal of Fluids and Structures* 28 (Jan. 2012), pp. 434–455. ISSN: 0889-9746. DOI: 10.1016/J.JFLUIDSTRUCTS.2011.11.001.

[14] JM Kirshner. *Design theory of fluidic components*. 1975. ISBN: 0124102506, 9780124102507.

[15] M Kubrak. "Water hammer phenomenon in pipeline with inserted flexible tube". In: *ascelibrary.org* (2020). URL: https://ascelibrary.org/doi/abs/10.1061/%28ASCE%29HY.1943-7900.0001673.

[16] P. Lafon et al. "Aeroacoustical coupling in a ducted shallow cavity and fluid/structure effects on a steam line". In: *Journal of Fluids and Structures* 18 (6 Dec. 2003), pp. 695–713. ISSN: 0889-9746. DOI: 10.1016/J.JFLUIDSTRUCTS.2003.08.018.

[17] Marshall Long. “Architectural Acoustics: Second Edition”. In: *Architectural Acoustics: Second Edition* (2014), pp. 1–950. DOI: 10.1016/C2009-0-64452-4. URL: http://www.sciencedirect.com:5070/book/9780123982582/architectural-acoustics.

[18] *PCB Piezotronics, model 112A22*. URL: https://www.pcb.com/products?m=112a22.

[19] Franck Renaud et al. “A new identification method of viscoelastic behavior: Application to the generalized Maxwell model”. In: *Mechanical Systems and Signal Processing* 25 (3 Apr. 2011), pp. 991–1010. ISSN: 0888-3270. DOI: 10.1016/J.YMSSP.2010.09.002.

[20] E Rieutord. “Transient response of fluid viscoelastic lines”. In: (1982). URL: https://asmedigitalcollection.asme.org/fluidsengineering/article-abstract/104/3/335/409418.

[21] Allemang RJ. *Vibrations: Analytical And Experimental Modal Analysis*. University of Cincinnati, 1999.

[22] R H Munnig Schmidt, G Schitter, and J van Eijk. *The design of high performance mechatronics. High-tech functionality by multidisciplinary system integration*. IOS Press, 2011. ISBN: 978-1-60750-825-0.

[23] J. S. Stecki and D. C. Davis. “Fluid Transmission Lines—Distributed Parameter Models Part 1: A Review of the State of the Art”. In: *Proceedings of the Institution of Mechanical Engineers, Part A: Journal of Power and Energy* 200 (4 1986), pp. 215–228. ISSN: 20412967. DOI: 10.1243/PIME_PROC_1986_200_032_02.

[24] L Suo and EB Wylie. “Complex wavespeed and hydraulic transients in viscoelastic pipes”. In: (1990). URL: https://asmedigitalcollection.asme.org/fluidsengineering/article-abstract/112/4/496/410804.

[25] Nijveldt T. *Pneumatic Manifold Design | TU Delft Repositories*. 2015. URL: https://repository.tudelft.nl/islandora/object/uuid:c20aed66-9c23-4d85-bc85-3543b373a75e.

[26] Bo Tan and Lyndon Scott Stephens. “Evaluation of viscoelastic characteristics of PTFE-Based materials”. In: *Tribology International* 140 (Dec. 2019), p. 105870. ISSN: 0301-679X. DOI: 10.1016/J.TRIBOINT.2019.105870.

[27] Devis Tonon et al. “Aeroacoustics of Pipe Systems with Closed Branches”. In: *http://dx.doi.org/10.1260/1475-472X.10.2-3.201* 10 (2-3 June 2011), pp. 201–275. ISSN: 1475-472X. DOI: 10.1260/1475-472X.10.2-3.201. URL: https://journals.sagepub.com/doi/10.1260/1475-472X.10.2-3.201.

[28] JS Walker and JW Phillips. “Pulse propagation in fluid-filled tubes”. In: (1977). URL: https://asmedigitalcollectic
asme.org/appliedmechanics/article-abstract/44/1/31/388759.

[29] F Yu et al. “Effect of phenyl content, sample thickness and compression on damping performances of silicone rubber: A study by dynamic mechanical analysis and impact”. In: *Elsevier* (2019). URL: https://www.sciencedirect.com/science/article/pii/S014294181931089X?casa_token=vXQSDy8O0gEAAAAA:thp-jpUNxtddehxYW0arYLx9XG4SQVrhw04AUbWuqObbnmm4cnebFd_YVkU1sedQFjl5YEYGwoQ.

[30] Chen Zhang et al. “A study on mechanical and thermal properties of silicone rubber/EPDM damping materials”. In: *Journal of Applied Polymer Science* 119 (5 Mar. 2011), pp. 2737–2741. ISSN: 00218995. DOI: 10.1002/APP.31697.